REVERSIBLE INTERCONVERTED Cu^{+}/Cu^{+}-H SPECIES IN $CuMgAlO_x$ CATALYSTS FOR SELECTIVE HYDROGENATION OF FATTY ACID METHYL ESTERS TO FATTY ALCOHOLS

CHANISARA NOOTO

A THESIS SUBMITTED IN PARTIAL FULFILLMENT OF THE REQUIREMENT FOR THE DEGREE OF MASTER OF SCIENCE IN APPLIED CHEMISTRY

DEPARTMENT OF CHEMISTRY SCHOOL OF SCIENCE
KING MONGKUT'S INSTITUTE OF TECHNOLOGY LADKRABANG

2025
KMITL-2025-SC-M-012-045

Thesis Title	Reversible interconverted Cu^{+}/Cu^{+}-H species in $CuMgAlO_x$ catalysts for selective hydrogenation of fatty acid methyl esters to fatty alcohols
Student Name	Chanisara Nooto
Student ID	64605030
Degree Department	Master of Science (Applied Chemistry)
Year	2025
Thesis Advisor	Assoc. Prof. Dr. Kittisak Choojun
Thesis Co-advisor	Prof. Dr. Tawan Sooknoi

Abstract

Selective fatty alcohol production (>90% selectivity) can be achieved by the selective hydrogenation of fatty acid methyl esters over layered double hydroxide derived $CuMgAlO_x$ catalysts in a fixed-bed reactor at 250 °C under atmospheric H_2. ~17wt.% Cu loading CuLDHs with different Mg^{2+}/Al^{3+} ratios ($CuMg_{60}Al_{40}O_x$, $CuMg_{70}Al_{30}O_x$, $CuMg_{75}Al_{25}O_x$, and $CuMg_{80}Al_{20}O_x$) were prepared by co-precipitation-hydrothermal method. The Cu dispersion and Cu species were determined by H_2-TPR, consecutive H_2-TPR, N_2O-dissociative reaction, and *in situ* TR-XANES. Highly dispersed Cu metal along with cationic Cu(I) species were obtained for all $CuMgAlO_x$. The cationic Cu(I) species (Cu^{+}/Cu^{+}-H) content increased with Mg^{2+} content. In the presence of H_2, the cationic Cu(I) species undergo reversible interconversion between Cu^{+} and Cu^{+}-H species, facilitating hydrogen dissociation/evolution. The hydrogenation activity was governed by the balance of the metallic Cu surface and the cationic Cu(I) species. The Cu^{+} species allow preferential adsorption of C=O ester for selective hydrogenation of FAMEs to fatty alcohol (>90% selectivity). With $Cu_{surface}/Cu(I)$ ratio at 0.25 ($CuMg_{75}Al_{25}O_x$), the fatty alcohol production rate of 49.3 h^{-1} was obtained with high stability due to the reversible interconversion of Cu^{+}/Cu^{+}-H that prevented product re-adsorption and side reactions.

Keywords: Cationic Cu(I) species, reversible interconversion, Cu^{+}/Cu^{+}-H species, CuLDHs, fatty alcohol, FAMEs, selective hydrogenation

Acknowledgments

I would like to take this opportunity to express my heartfelt gratitude to my advisors, Assoc. Prof. Dr. Kittisak Choojun and co-advisor Prof. Dr. Tawan Sooknoi, for their invaluable guidance, profound knowledge, and insightful discussions throughout the course of this work. Their continual support and encouragement have been instrumental in the completion of this project. I extend my sincere appreciation to the chairperson, Dr. Yingyot Poo-arporn, and the committee members, Assoc. Prof. Dr. Panpailin Seeharaj, for their constructive feedback and expert guidance, which have significantly enriched this work.

This research was made possible through the support of King Mongkut's Institute of Technology Ladkrabang (KMITL) and funding provided by the National Research Council of Thailand (NRCT) and King Mongkut's Institute of Technology Ladkrabang (KMITL) under project number N42A660796. Additionally, I am deeply grateful to the Synchrotron Light Research Institute (Public Organization), Thailand, for providing access to in situ TR-XANES experiments at Beamline 2.2, and to the Scientific Instruments Center, School of Science, KMITL, for their assistance with advanced characterizations. I would also like to extend my thanks to the Catalytic Chemistry Research Unit members for their valuable contributions, insightful ideas, and unwavering support throughout this journey.

Furthermore, I am profoundly thankful to the Department of Chemistry, School of Science, King Mongkut's Institute of Technology Ladkrabang, for providing access to advanced laboratory instruments, equipment, chemicals, and facilities.

Lastly, and most importantly, I am deeply grateful to my parents and family for their unconditional love, encouragement, and unwavering support, which have been a constant source of strength and motivation throughout this endeavor.

Miss Chanisara Nooto

Table of contents

Table of contents (continued)

List of tables

List of figures

Figures **Page**

List of figures (continued)

Figures **Page**

List of figures (continued)

List of schemes

Schemes **Page**

Abbreviations/Symbols

°C	Degree Celsius
XRD	X-Ray Diffraction
TPR	Temperature-Programmed Reduction
TPD	NH_3-Temperature Programmed Desorption
BET	Brunauer-Emmett-Teller method
ICP-MS	Inductively coupled plasma mass spectrometry
TEM	Transmission electron microscopy
FAMEs	Fatty acid methyl esters
TCD	Thermal conductivity detector
LDHs	Layered double hydroxides
CuLDHs	Copper layered double hydroxides
MP	Methyl palmitate
BAS	Brønsted acid site

Chapter 1
Introduction

1.1 Research motivation

Fatty alcohols, commonly referred to as long-chain alcohols (C12–C18), are vital industrial chemicals with diverse applications, including their use as surfactants, plasticizers, solvents, flavorings, detergents, foam stabilizers, and components in cosmetics, plastic intermediates, paints, and coatings [1,2]. The global consumption of fatty alcohol exceeds 5,500 kilotons, representing a market value of approximately $8.5 billion [3,4]. Traditionally, fatty alcohols have been synthesized from petroleum-based feedstocks via hydroformylation followed by selective hydrogenation, employing CO, H_2, and paraffin as reactants [5–8]. However, these processes are neither environmentally sustainable nor aligned with the principles of green chemistry. As an alternative, bio-based fatty alcohols can be produced through the selective hydrogenation of fatty acid methyl esters (FAMEs), which are derived from renewable triglyceride sources such as vegetable oils (e.g., palm and soybean oils), waste cooking oils, and animal fats. Despite their alignment with carbon neutrality goals, the production costs of bio-based fatty alcohols ($2,500–$6,000 per metric ton) are significantly higher than those of their petroleum-derived counterparts ($1,500–$3,000 per metric ton) [9–12], resulting in higher profit margins for bio-based products. Therefore, the catalytic hydrogenation of FAMEs into fatty alcohols represents a crucial sustainable strategy for valorizing renewable feedstocks and advancing carbon-neutral production pathways [13,14].

Copper-chromite ($CuO/CuCr_2O_4$) catalysts are widely employed in industrial processes for the selective hydrogenation of fatty acid methyl esters (FAMEs) to fatty alcohols under elevated temperatures (200–400 °C) and high H_2 pressures (200–300 bar) [15–17]. However, the leaching of toxic chromium species under these harsh reaction conditions poses significant environmental and waste management challenges. Non-noble metal catalysts with lower toxicity, such as Ni/SiO_2 [18,19], $Ni-Fe/Al_2O_3$ [20], $Co/SiO_2-Al_2O_3$ [21], and Co/SiO_2 [22], have been investigated as alternatives. These catalysts, however, frequently promote decarbonylation reactions, producing olefinic products with a one-carbon shorter chain length, thereby reducing

alcohol selectivity. Additionally, their susceptibility to deactivation due to CO poisoning and coke formation limits their long-term catalytic efficiency. In contrast, despite the typically poor metal dispersion observed in impregnated Cu-based catalysts, these materials demonstrate minimal decarbonylation and decarboxylation activities and exhibit high selectivity toward fatty alcohol production, making them promising candidates for this transformation [23,24].

Achieving highly dispersed and stabilized Cu nanoparticles needs strong metal-support interactions or refined preparation techniques. However, Cu supported on conventional reducible metal oxides, such as TiO_2 and CeO_2, exhibits markedly low catalytic activity due to the electron deficiency induced at the Cu surface by these reducible oxides [24–29]. In contrast, copper phyllosilicate catalysts demonstrate exceptional Cu dispersion (>65%) on inert supports. This enhanced dispersion is attributed to the strong interaction between Cu and SiO_2 within the octahedral sites of chrysocolla-like structures, facilitating the formation of Cu^+ species retained within the catalyst framework [30–32]. The Cu^+ species are critical role in preventing Cu agglomeration, thereby maintaining high catalytic activity [30–34]. Furthermore, these Cu^+ species promote η^1-adsorption of the carbonyl (C=O) group, effectively suppressing decarbonylation and decarboxylation pathways. Additionally, Cu^+ species facilitate the desorption of produced alcohols while preventing their re-adsorption, thus enhancing alcohol selectivity [30,31]. However, Brønsted acid sites (BAS), originating from the interaction of silanol groups at Cu perimeters, can catalyze the dehydration of alcohols to olefins, reducing selectivity and causing catalyst deactivation [30]. Efforts to mitigate these side reactions through alkali metal doping to neutralize BAS have improved alcohol selectivity only up to ~60% [31].

Copper layered double hydroxides (CuLDHs) consist of positively charged brucite-like layers ($M(OH)_6$ octahedra, where M = Cu^{2+}, Mg^{2+}, and Al^{3+}) and interlayer anions. The Mg^{2+}/Al^{3+} ratio within these octahedral layers plays a crucial role in determining both the basicity of the CuLDHs and the interaction between Cu and the support (Cu-MgO and Cu-Al_2O_3) [35]. The strong interaction of Cu within the confined metal oxide sheets significantly influences Cu reducibility, the Cu^0/Cu^+ ratio generation, and Cu dispersion following reduction [33,36]. As a result, basic catalysts with highly dispersed Cu^0/Cu^+ species can be obtained from $CuMgAlO_x$ derived from CuLDHs, enabling high selectivity for fatty alcohol production via FAMEs hydrogenation.

Supporting this, Cui et al. demonstrated that $CuMgAlO_x$ catalysts derived from LDHs with a Mg^{2+}/Al^{3+} ratio of 1.0 achieved >99% selectivity for ethylene glycol during the selective hydrogenation of dimethyl oxalate [37].

The ultra-fine Cu nanoparticles with Cu^0/Cu^+ species confined within mixed oxide sheets exhibit distinct hydrogen dissociation, adsorption, and evolution behavior, as is typically observed for other M^0/M^+ systems. For instance, AgHZSM-5 demonstrates reversible interconversion between Ag^0 and Ag^+ under hydrogenation conditions [38]. Exchangeable Ag^+ is reduced to Ag^0 in the presence of H_2, with proximal Brønsted acid sites (BAS) facilitating the process. Dissociated hydrogen on Ag^0 can react reversibly with BAS to regenerate Ag^+, releasing H_2 under inert conditions. Similarly, dimeric extra-framework gallium species ($[Ga_2O_2]^{2+}$) are capable of dissociating hydrogen to form Ga^+-H species, which reversibly evolve hydrogen in inert environments [39]. For Cu-containing LDHs, heterolytic hydrogen dissociation has been proposed, forming $Cu\delta^+$-H species [32]. The reversible interconversion of Cu^+-H species in LDH-derived $CuMgAlO_x$ catalysts is particularly effective in promoting the selective hydrogenation of carbonyl compounds (e.g., aldehydes and esters), akin to the behavior of classical hydride species. Additionally, the simultaneous dissociation and evolution of hydrogen on the catalyst surface suppress carbon deposition, thereby extending the catalyst's operational lifetime.

With this regard, the selective hydrogenation of methyl palmitate (MP) to long-chain alcohol (hexadecanol) over LDHs derived $CuMgAlO_x$ catalysts was investigated in a continuous fixed-bed reactor under atmospheric H_2 pressure. 17wt.% CuLDHs with various Mg^{2+}/Al^{3+} ratios were tested for structural stability, reducibility, and Cu dispersion. The Cu^+/Cu^0 species and their reversible interconversion were characterized by consecutive H_2-TPR, N_2O-dissociative reaction, and *in situ* TR-XANES, from which the corrected Cu dispersion could be determined. The effect of Mg^{2+}/Al^{3+} on Cu^+/Cu^0 species and selective hydrogenation activity was explored. In addition, the role of cationic Cu(I) species in LDHs derived $CuMgAlO_x$ on the alcohol selectivity and stability was evaluated. The balance between metallic Cu surface and cationic Cu(I) species for the production of long-chain alcohol was also highlighted.

1.2 Objectives of the study

1.2.1 To synthesize long-chain alcohols from fatty acid methyl esters via hydrogenation.

1.2.2 To evaluate the catalytic performance of CuLDHs in the hydrogenation reaction.

1.2.3 To investigate the influence of the Mg:Al ratio on the properties and activity of CuMgAl-LDH catalysts.

1.2.4 To determine the optimal reaction conditions for the hydrogenation process.

1.3 Scopes of the study

1.3.1 Preparation of catalysts: The catalyst of Cu loading of 20% over MgAl-LDHs catalysts.

1.3.2 Cu based catalyst: Effect of the Mg/Al ratio for synthesis

1.3.3 Characterization of catalysts: The catalysts will be characterized by the following techniques:

1.3.3.1 X-ray diffraction techniques (XRD)

1.3.3.2 Thermogravimetric analysis (TGA)

1.3.3.3 N_2 adsorption-desorption analysis: Brunauer–Emmett–Teller (BET) and Barrett-Joyner-Halenda (BJH) method

1.3.3.4 Transmission electron microscopy (TEM)

1.3.3.5 NH_3 temperature program desorption (NH_3-TPD)

1.3.3.6 Temperature program reduction (H_2-TPR)

1.3.3.7 Dissociative N_2O adsorption technique temperature program reduction (N_2O-TPR)

1.3.3.8 *In situ* time-resolved X-ray absorption near edge spectroscopy (*in situ* TR-XANES)

1.3.3.9 Inductively coupled plasma atomic emission spectroscopy (ICP-OES)

1.3.4 Reaction test: The selective hydrogenation of methyl palmitate will be investigated in the fixed-bed reactor under an H_2 atmosphere with the contact time of 374 g.mol/h at the reaction temperatures of 250 °C.

1.3.5 The analysis of the liquid products is performed using a gas chromatograph (GC) coupled with a flame ionization detector (FID).

1.4 Benefits of the study

To develop a highly efficient Cu-based catalyst with high Cu dispersion for the hydrogenation of palmitic acid, achieving high selectivity for hexadecanol production.

Chapter 2

Theory and literature reviews

2.1 Palm oil

Palm oil is one of the most significant vegetable oils worldwide, and Thailand plays a key role in its production, catering primarily to the domestic market and export. It is extensively used in food products, cosmetics, and biofuels. Thailand ranks among the largest palm oil producers in Asia, following Indonesia and Malaysia [40,41]. The country has a well-established palm oil industry, producing both crude palm oil (CPO) and refined palm oil (RPO). Thailand's annual palm oil production is estimated at approximately 3.5 to 4 million metric tons, with expectations for future growth (**Figure. 2.1**). Palm oil is widely utilized across various sectors, including food, biodiesel, cosmetics, and other industrial applications [42,43].

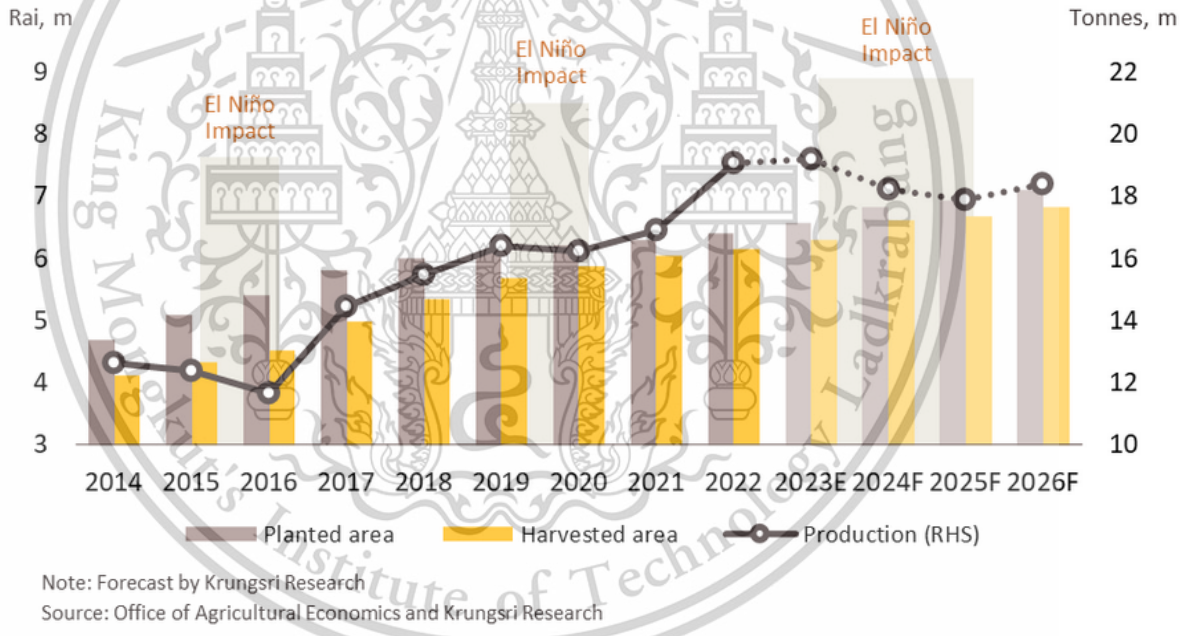

Figure 2.1 Thai palm oil plantation area and production volume.

2.2 Fatty acid methyl ester (FAMEs)

Fatty Acid Methyl Esters (FAMEs) are essential in the production of biodiesel, providing a renewable energy source with significant environmental, economic, and sustainability benefits. By utilizing renewable feedstocks like vegetable oils, animal fats, and waste oils, FAME-based biodiesel offers an environmentally friendly alternative to petroleum fuels, delivering energy content comparable to conventional

diesel. In addition, it contributes to reducing carbon emissions and enhancing energy security [13,14]. FAMEs consist of both saturated fatty acids (such as palmitic acid and stearic acid) and unsaturated fatty acids (including oleic acid, linoleic acid, and linolenic acid) [44,45]. The production of FAMEs involves the transesterification of triglycerides with methanol, catalyzed by either an acid or base catalyst, as illustrated in **Scheme 2.1** [46]

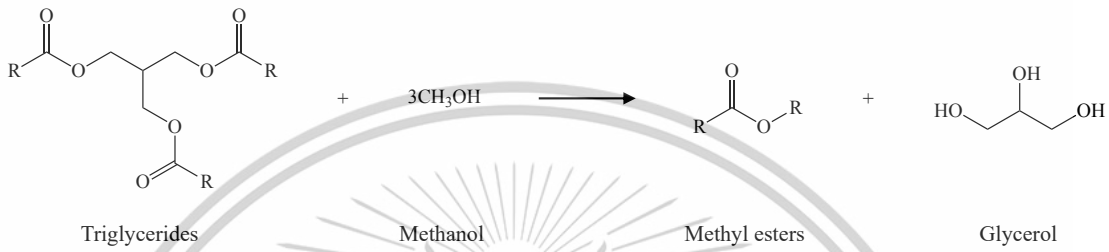

Scheme 2.1 Transesterification of triglyceride.

2.3 Methyl palmitate

Methyl palmitate ($C_{17}H_{34}O_2$) is a methyl ester derived from palmitic acid, which occurs naturally in sources such as palm oil, coconut oil, and animal fats. It is one of the fatty acid methyl esters produced during the transesterification process in biodiesel production, where triglycerides react with methanol in the presence of a base catalyst to form biodiesel (fatty acid methyl esters) [47]. The chemical structure of methyl palmitate is shown in **Scheme 2.2** [48].

Scheme 2.2 chemical structure of methyl palmitate.

Additionally, methyl palmitate serves as an emollient, contributing to the softening and smoothing of the skin, making it a common ingredient in formulations such as moisturizers, creams, lotions, and lip balms. In pharmaceutical applications, it functions as a solvent for active ingredients in ointments and topical creams. Methyl palmitate is also utilized as a solvent, lubricant, and plasticizer in various industrial applications.

Table 2.1 The chemical and physical properties of hexadecanol.

Properties	Values
IUPAC Name	Methyl hexadecanoate
Molecular Formula	$C_{17}H_{34}O_2$
Molecular Weight (g/mol)	270.44 g/mol
Physical Description	Liquid at room temperature
Color/Form	Colorless liq
Boling Point (°C)	417
Melting point (°C)	30
Density (g/ml)	0.852 at 25 °C
Solubility	Soluble in alcohol, acetone, chloroform and benzene, soluble in ether. Insoluble in water.
Vapor Pressure (mmHg)	6.04e-05

2.4 Fatty alcohol or long chain alcohol

Fatty alcohols are a class of alcohols derived from natural fats and oils. These alcohols have long carbon chains, usually ranging from 12 to 22 carbon atoms. They are typically produced by hydrogenating fatty acids or triglycerides, which are found in both vegetable oils and animal fats. Fatty alcohols are widely used in various industries, including cosmetics and personal care products, where they function as emulsifiers and thickeners. They are also utilized as lubricants, corrosion inhibitors, detergents, cleaning agents, and plasticizers in the production of plastics and resins [1,2].

2.5 Hexadecanol

Hexadecanol, also known as cetyl alcohol, is a fatty alcohol with the chemical formula $C_{16}H_{34}OH$. Hexadecanol is primarily obtained from natural sources, such as palm oil, through processes like hydrogenation of methyl palmitate. Hexadecanol is commonly used in the pharmaceutical, surfactants, plasticizers, industrial applications, cosmetics, and personal care. The structure of 1-hexadecanol is shown in **Scheme 2.3** [49].

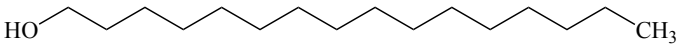

Scheme 2.3 chemical structure of 1-hexadecanol.

Table 2.2 The chemical and physical properties of hexadecanol.

Properties	Values
IUPAC Name	Hexadecan-1-ol
Molecular Formula	$C_{16}H_{34}O$
Molecular Weight (g/mol)	242.44 g/mol
Physical Description	Flake form at room temperature
Color/Form	White
Boling Point (°C)	344
Melting point (°C)	49.3
Flash Point (°C)	175
Solubility	Soluble in alcohol, chloroform, and ether. Insoluble water
Vapor Pressure (mmHg)	4.70e-05

2.6 Layered double hydroxides (LDHs)

Layered Double Hydroxides (LDHs), often referred to as hydrotalcite-like compounds, derive their name from their structural similarity to the mineral hydrotalcite. LDHs are made up of positively charged metal hydroxide layers, which are separated by an interlayer space that contains intercalated anions and water molecules. These materials have a general formula of: $[(M^{II})_{1-x}(M^{III})_x(OH)_2]^{x+}(A^{m-}{}_{x/m})\cdot nH_2O]$. In this formula, M^{2+} represents divalent metal ions (such as Mg^{2+}, Zn^{2+}, Fe^{2+}), while M^{3+} denotes trivalent metal ions (such as Al^{3+}, Cr^{3+}, Fe^{3+}). A^{n-} refers to the intercalated anions (e.g., CO_3^{2-}, NO_3^-, Cl^-, SO_4^{2-}), and x is the mole ratio of M^{3+} to the total metal cation content ($M^{2+}+M^{3+}$) [50,51]. The structural arrangement of LDHs is depicted in **Scheme 2.4.**

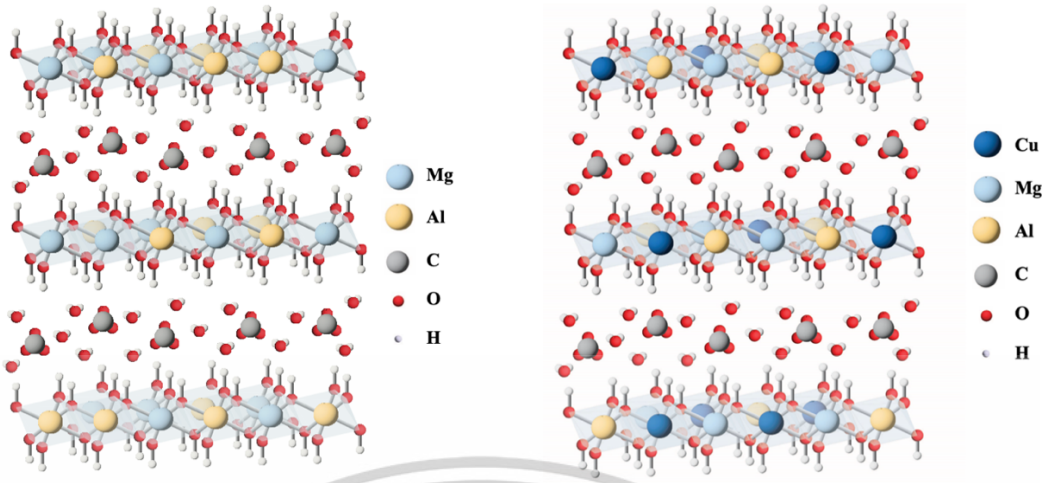

Scheme 2.4. Structure of layered double hydroxide structure

Copper Layered Double Hydroxides (Cu-LDHs) are a type of Layered Double Hydroxides (LDHs) in which copper ions (Cu^{2+}) are incorporated into the hydroxide layers along with other metal ions. While Cu-LDHs share many structural and chemical features with other LDHs, the presence of copper imparts distinctive properties, such as enhanced catalytic activity, particularly in hydrogenation reactions. Cu-LDHs can be synthesized through various methods, including co-precipitation [52–54] and the separate nucleation and aging step (SNAS) method [55]. In this study, CuMgAl-LDHs were synthesized using both the co-precipitation and hydrothermal techniques [32]. A key characteristic of Cu-LDHs is the layered arrangement of metal hydroxides, where copper ions are coordinated with hydroxyl groups to form a stable structure. After reduction, copper can be highly dispersed on MgAl-LDHs, enhancing their catalytic performance.

2.7 Literature reviews

Fatty alcohols are a group of long-chain alcohols primarily derived from natural fats and oils. These alcohols have diverse applications in industries such as cosmetics, personal care, detergents, plastics, and lubricants [1].

The production of long-chain alcohols can be achieved sustainably through the selective hydrogenation of Fatty Acid Methyl Esters (FAMEs) [30]. These fatty alcohols are derived from triglycerides found in renewable resources such as vegetable oils (including palm and soybean oil), waste cooking oils, and animal fats. In light of the ongoing push for carbon neutrality, bio-based fatty alcohols are currently priced

between $2,500 and $6,000 per metric ton, which is approximately double the cost of their petroleum-based counterparts, priced between $1,500 and $3,000 per metric ton [9–12]. In Thailand, a significant portion of FAMEs is sourced from palm oil, which represents nearly 80% of the market's crop production. Methyl palmitate, a saturated methyl ester, is primarily produced through the transesterification of palm oil, accounting for about 45% of the total output. This compound can be transformed into various intermediate chemicals, including fatty aldehydes, fatty alcohols, long-chain α-olefins, and long-chain hydrocarbons.

The traditional method for producing long-chain alcohols involves the selective hydrogenation of fatty acid methyl esters (FAMEs). Several supported metal catalysts, such as $CuO/CuCr_2O_4$, are known to achieve high conversion rates and selectivity for alcohols. Which, Ross D. Rieke *et. al.* (1997) studied the hydrogenation of fatty methyl esters to fatty alcohol using a $CuO/CuCr_2O_4$ catalyst in a batch reactor. The process was conducted at 280 °C and under hydrogen gas at 138 bar pressure for 8 h. They found that the catalysts achieved a conversion rate of 98%, with an alcohol selectivity of 95% [56]. The $CuCr_2O_4$ catalyst operated under the challenging conditions of high temperature and high pressure.

However, these catalysts operate under harsh conditions. In contrast, catalysts like Ni/SiO_2 [18,19], $Ni\text{-}Fe/Al_2O_3$ [20], $Co/SiO_2\text{-}Al_2O_3$ [21], and Co/SiO_2 [22] have also been found to be effective for this hydrogenation process. Nonetheless, these catalysts often promote decarbonylation, which leads to the formation of olefinic products with shorter carbon chain lengths. As a result, this side reaction reduces the selectivity for alcohol production.

In a study conducted by Mathias S. *et al.* (2006), the deoxygenation of stearic acid using a catalyst of over 60% Ni/SiO_2 was investigated in a batch reactor. The experiment was carried out at 300 °C under a pressure of 6 bars of helium gas for a duration of 4 h. The results indicated that the catalyst achieved an 18% conversion rate with a hexadecane selectivity of 58% [18]. The nickel catalyst also facilitated decarboxylation, resulting in the production of long-chain hydrocarbons with carbon dioxide (CO_2) being released as a byproduct.

Kong *et. al.* studied the bimetallic Ni-Fe catalyst for the hydrogenation of stearic acid to produce stearic alcohol in a batch reactor at 250 °C 5 h under 5 Mpa of H_2 pressure [20]. They found the $Ni_{1.8}Fe_{1.5}$ give a high conversion of 99% with high stearic

alcohol 98%. However, the catalyst required a relatively high reduction temperature (650 °C) leading to the sintering of the catalyst. In addition, they found that the conversion could not observed over Fe carbon coated catalyst. Therefore, finding the right metal catalyst under optimal reaction conditions is challenging.

R. Krishnapriya *et al.* (2012) investigated the hydrogenation and hydrodeoxygenation of methyl oleate using 6% Co/SiO_2-$Al2O_3$ catalysts at under a hydrogen pressure of 20 bar for 10 h. They discovered that these catalysts achieved 100% conversion with 51% C-17 and 42% C-18 selectivity [21]. These clearly show that the catalyst also selectively promotes decarboxylation, and over hydrogenation also occurs.

Phichitsurathaworn P. *et al.* (2020) conducted a study on the deoxygenation of heptanoic acid to hexene using a 5% Co/SiO_2 fixed-bed reactor at 400 °C under atmospheric pressure of H_2 gas. They found the catalyst provided 84.7%conversion with a hexene yield of 46%. Also, the cracking products (C1-C5) were obtained ~19%. In addition, they found the deactivation activity after 6 h [22]. Additionally, this cobalt catalyst facilitates decarboxylation, resulting in the production of long-chain hydrocarbons through the release of carbon dioxide (CO_2).

Xiaohai Z. *et. al.* (2023) studied the hydrogenation of methyl palmitate to hexadecanol over CuO catalysts in a batch reactor at 300 °C under 7.5 bar of H_2 gas for 2 h. The research observed that the catalysts show 2.6% conversion with 88.5% hexadecanol selectivity, due to the larger Cu crystallite size. This could be attributed to the agglomerate of Cu.

These catalysts often promote decarbonylation, leading to olefinic products that have a chain length one carbon shorter, which decreases the selectivity for alcohol production. Additionally, they are vulnerable to CO poisoning and deactivation due to coke formation, further limiting their long-term efficiency. In contrast, traditional CuO catalysts exhibit better selectivity for alcohols, but they suffer from low activity because of poor metal dispersion.

Prasanseang W. *et al.* (2022) described the preparation of a copper (Cu) phyllosilicate catalyst using the ammonia evaporation method, resulting in a catalyst with a 20% Cu loading. This method produced a catalyst with a high surface area of 344 m^2/g with high Cu dispersion (72.9 %). [30]. The high Cu dispersion could be attributed to the strong interaction between Cu and SiO_2, resulting in the presence of

both Cu^{+} and Cu^{0} mixture. The reaction was conducted in a fixed-bed reactor at a temperature of 250 °C, utilizing a 10 wt% solution of methyl palmitate in dodecane with a hydrogen flow rate of 180 mL/min. The 20CuPS catalyst achieved a high conversion rate of 73.2%, but it demonstrated a greater selectivity for hexadecane at 41.7% compared to hexadecanol, which was 19.2%. This preference can be attributed to the Brønsted acid sites formed on the CuPS after reduction, which promote the dehydration of hexadecanol, leading to hexadecane as the main product.

Cui *et al.* (2019) investigated the use of CuMgAl layer double hydroxides (CuMgAl-LDHs), which were prepared using a method that involved separate nucleation and aging steps, for the hydrogenation of dimethyl oxalate to ethylene glycol [37]. Their findings demonstrated that the $CuMgAlO_x$ (with a Mg^{2+}/Al^{3+} ratio of 1.0) derived from these LDHs achieved over 99% conversion of dimethyl oxalate into ethylene glycol through selective hydrogenation. This catalyst possesses Lewis acid and base sites but lacks Brønsted acid sites, which distinguishes it from Cu/Al_2O_3, a catalyst that does contain Brønsted acid sites. The study indicated that Cu/Al_2O_3 primarily produces methyl glycolate, whereas CuMgAl-LDHs mainly yield ethylene glycol. This difference suggests that the absence of Brønsted acid sites in CuMgAl-LDHs inhibits the formation of dehydration products. Moreover, the Lewis acid sites in CuMgAl-LDHs promote the η^1-C=O adsorption, thereby enhancing conversion rates. Consequently, the basic catalysts containing highly dispersed Cu^0/Cu^+ species can be obtained from LDHs derived from $CuMgAlO_x$, leading to a high selectivity for fatty alcohols produced from the hydrogenation of fatty acid methyl esters (FAMEs). Additionally, the catalyst's physical properties are influenced by various preparation parameters, including the Cu+Mg/Al molar ratio, Cu loading, and calcination temperature. The strong interaction between Cu and the support, along with tunable acid sites, allows CuMgAl-LDHs to suppress the dehydration of alcohols during the reaction effectively.

The ultra-fine copper (Cu) nanoparticles, which contain both Cu^0 and Cu^+ within the confined mixed oxide sheets, exhibit unique behaviors in terms of hydrogen dissociation, adsorption, and evolution. These behaviors resemble those observed in M^0/M^+ species. For instance, Ausavasakhi et al. have demonstrated that AgHZSM-5 can reversibly interconvert [38]. Their study on the reversible interconversion in AgHZSM-5(28) shows that cationic Ag clusters, formed at 425 °C, can switch between different oxidation states or ionic and metallic forms at temperatures below 425 °C.

This process is Influenced by temperature and the presence of hydrogen. However, metallic Ag clusters in AgHZSM-5(11) are more stable and do not undergo this interconversion, even at higher temperatures. The zeolite's framework and the presence of hydrogen contribute to the stabilization of the interconverted species, impacting their catalytic behavior, particularly in reactions that require hydride transfer or hydrogenation.

Chapter 3

Research methodology

3.1 Reagents

Details on the reagents used in this research are summarized in **Table 3.1**.

Table 3.1 A list of reagents.

Chemical	Grade of purity	Manufactuter
Copper(II) nitrate trihydrate ($Cu(NO_3)_2 \cdot 6H_2O$)	99.50%	QREC
Magnesium nitrate hexahydrate ($Mg(NO_3)_2 \cdot 6H_2O$)	98.00%	PANREAC APPLI-CHEM
Aluminium nitrate nonahydrate ($Al(NO_3)_2 \cdot 9H_2O$)	98.00%	PANREAC APPLI-CHEM
Sodium hydroxide anhydrous pellet (NaOH)	98.00%	CARLO ERBA
Sodium carbonate anhydrous (Na_2CO_3)	99.50%	CARLO ERBA
Mwthanol (CH_3OH)	99.90%	CARLO ERBA
Methyl palmitate ($C_{17}H_{32}O_2$)	97.00%	SIGMA-ALDRICH
n-dodecane ($C_{12}H_{26}$)	99.90%	CARLO ERBA
n-octane (C_8H_{18})	99.90%	CARLO ERBA
n-heptane ($C_{17}H_{16}$)	99.90%	CARLO ERBA
Hydrogen	99.99%	UIG company
Nitrogen	99.99%	UIG company
Air (zero grade)	99.99%	UIG company
10% hydrogen in argon	99.98%	UIG company
Helium	99.999%	UIG company
1% hydrogen in argon	99.98%	Linde
1% ammonia in helium	99.99%	Linde

3.2 Apparatuses

3.2.1. Glass bead

3.2.2. Glass wool

3.2.3. Glass syringe, SGE Analytical Science

3.2.4. GC needle, SGE Analytical Science

3.2.5. Graduate pipette and bulb

3.2.6. Laboratory glassware

3.2.7. Stirrer and heater

3.2.8. Protector laboratory hood, Science Technology

3.2.9. Quartz wool

3.2.10. Quartz tube

3.2.11. Furnace, Utsakan No. SCG-14

3.2.12. Powder X-ray diffractometer

3.2.13. Gas chromatography, Agilent Technologies 7890B

3.2.14. Borosilicate glass tube

3.2.15. Glass rod

3.2.16. Saturator

3.2.17. Syringe pump

3.2.18. Surface area and pore size analyzer, TOP200, Altermira Instruments

3.2.19. Alumina crucible

3.2.20. Agate mortar

3.2.21. Thermogravimetric analyzer, Pyris, Perkin Elmer

3.3 Catalyst preparation

Copper-containing layered double hydroxides (CuLDHs, ~17 wt.%) were synthesized via co-precipitation and hydrothermal methods, following the protocol described previously [32], with varying Mg^{2+}/Al^{3+} ratios. A fixed amount of copper(II) nitrate trihydrate ($Cu(NO_3)_2 \bullet 3H_2O$, 2.20 g) was used for all samples. The corresponding masses of magnesium nitrate hexahydrate ($Mg(NO_3)_2 \bullet 6H_2O$) and aluminum nitrate nonahydrate ($Al(NO_3)_3 \bullet 9H_2O$) employed for $CuMg_{60}Al_{40}O_x$, $CuMg_{70}Al_{30}O_x$, $CuMg_{75}Al_{25}O_x$, and $CuMg_{80}Al_{20}O_x$ were 6.32:9.25, 7.12:8.33, 7.83:7.50, and 8.77:6.42, respectively. The metal precursors were dissolved in 200 mL of a 50% (v/v) methanolic solution

(solution A). Separately, 0.0142 g/mL sodium carbonate (Na_2CO_3) and 0.0177 g/mL sodium hydroxide (NaOH) were dissolved in 200 mL of the same methanolic solution to prepare solution B, which was used to control the pH during the formation of CuLDHs. Solutions A and B were simultaneously added dropwise at a rate of 2 mL/min into 200 mL of methanolic solution under vigorous stirring, maintaining the pH at 10 ± 0.3 (**Figure 3.1**). The resulting suspension was stirred at the same pH for an additional 10 minutes before being transferred to a 1 L HDPE bottle for aging at 65 °C for 24 h without stirring. The aged solid was filtered, washed with deionized water until neutral pH, and dried at 90 °C for 24 h, yielding the precursor material, denoted as $CuMgAlO_x$-pre. The precursor was subsequently calcined under airflow (60 mL/min) at 550 °C (heating rate of 2 °C/min) for 12 h to produce mixed metal oxide catalysts, denoted as $CuMgAlO_x$. Prior to catalytic evaluation, all $CuMgAlO_x$ catalysts were reduced at 250 °C under a flow of H_2 gas (60 mL/min) for 2 h.

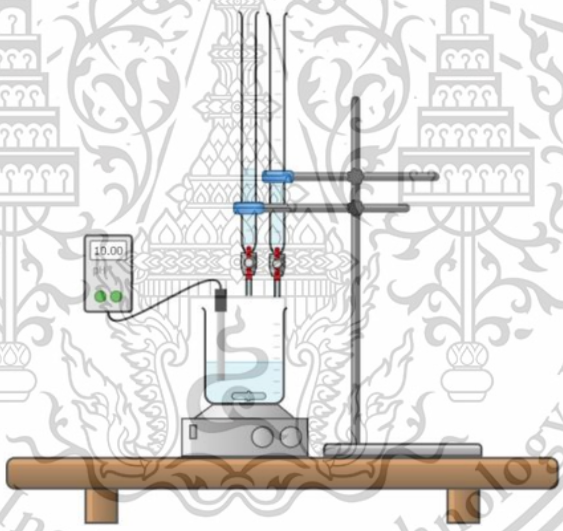

Figure 3.1 a) A solution containing mixed metals (stock solution A), and b) a solution acting as a base (stock solution B).

3.4 Catalysts characterization

The surface area of the samples was determined using an N2 adsorption-desorption analyzer (TOP200, Altermira Instruments) following the Brunauer–Emmett–Teller (BET) method. Approximately 50 mg of the sample was degassed at 100 °C for 12 h before introducing N_2 at -196 °C for the adsorption-desorption experiment. Elemental compositions of copper (Cu), magnesium (Mg), and aluminum (Al) were

quantified via inductively coupled plasma-optical emission spectrometry (ICP-OES, Avio 500 Max, PerkinElmer). A 0.05 g sample was digested in a solution containing 30 mL of H_2SO_4 and 15 mL of HNO_3, heated to 210 °C for 12 h at a rate of 2 °C/min. Post-digestion, the solution was filtered, diluted with deionized water, and analyzed.

Thermal stability and weight loss of the samples were assessed using thermogravimetric analysis (TGA/DSC1, Mettler Toledo). Approximately 30 mg of the sample was heated under a N_2 atmosphere from 50 to 900 °C at 10 °C/min. X-ray powder diffraction (XRD) (SmartLab, Rigaku) was employed to determine structural features and crystallite sizes using Cu K_α radiation (1.54441 Å), a Kβ filter (0.4970), a step width of 0.010°, and a scan speed of 50°/min with a total acquisition time of 2 min. Morphological and topological characteristics were investigated by transmission electron microscopy (TEM) using a TECNAI G2 20 (FEI) equipped with energy-dispersive X-ray spectroscopy (EDX) mapping. For TEM analysis, ~10 mg of the sample was dispersed in ethanol and sonicated for 1 min, and 50 µL of the suspension was deposited on a carbon film-supported nickel grid and dried at ambient conditions.

Acid strength and acidity were evaluated using NH_3 temperature-programmed desorption (NH_3-TPD) on a custom-made instrument equipped with a thermal conductivity detector (TCD, VICI Valco Instrument). Prior to NH_3-TPD, ~50 mg of the $CuMgAlO_x$ catalyst was reduced under H_2 flow (60 mL/min) at 250 °C for 2 h at a heating rate of 10 °C/min. After cooling to room temperature, the catalyst was exposed to 1% NH_3/Ar (60 mL/min) for 1 h, followed by He flushing to remove physisorbed NH_3. Desorption was monitored by heating from 50 to 900 °C at 10 °C/min. The TCD signal was recorded in both the heating and cooling steps and calibrated using HZSM-5 as a standard.

The reducibility of the samples was assessed using H_2 temperature-programmed reduction (H_2-TPR) with a custom-made instrument equipped with a thermal conductivity detector (TCD, VICI Valco Instrument). Approximately 50 mg of the $CuMgAlO_x$ sample was first calcined in the air (flow rate: 60 mL/min) at 550 °C for 12 h with a heating rate of 2 °C/min. After calcination, the sample was cooled to room temperature under a nitrogen atmosphere. The H_2-TPR analysis was performed by heating the sample under a 10% H_2/Ar gas flow (60 mL/min) from 80 to 900 °C at a rate of 10 °C/min. The TCD signal was recorded during both the heating and cooling steps. Calibration of the TCD response was carried out using CuO as a standard.

Additionally, a standard pulse containing 1% H_2/Ar was injected after each H2-TPR analysis for validation and quantification purposes.

The dissociated N_2O adsorption technique was utilized to estimate copper (Cu) dispersion, following a methodology similar to H_2-TPR. Initially, the $CuMgAlO_x$ sample was calcined at 550 °C with a heating rate of 2 °C/min. The first H_2-TPR analysis was then conducted by heating the sample from 80 °C to 350 °C at 10 °C/min under a 10% H_2/Ar flow (60 mL/min) and maintaining the temperature at 350 °C for 2 hours to determine the initial H_2 consumption, during which all copper species were reduced. Subsequently, the sample was cooled to 60 °C under a nitrogen flow (60 mL/min), and the catalyst surface was oxidized using N_2O (60 mL/min) at 60 °C for 1 hour. Excess N_2O was then flushed out by flowing nitrogen at 100 °C for 1 hour, after which the sample was cooled to room temperature. A secondary H_2-TPR analysis was performed under identical conditions to the first H_2-TPR. The hydrogen consumption data obtained from the primary and secondary H_2-TPR analyses were used to calculate the dispersion of copper on the surface. The Cu dispersion was determined using the equation provided in **Figure A5** [57].

Consecutive H_2-TPR measurements were conducted using a custom-made instrument equipped with a thermal conductivity detector (VICI, Valco instrument) to investigate the reversible interconversion of Cu^+/Cu^+-H species in the $CuMgAlO_x$ catalysts. Approximately 50 mg of the $CuMgAlO_x$ sample was ground to a 20-mesh particle size and packed into a quartz tube placed in the reactor's heating zone. Initially, the sample was recalcined in an air flow (60 mL/min) at 550 °C for 12 hours at a heating rate of 2 °C/min. Following calcination, the sample was cooled to room temperature under a nitrogen atmosphere. The first H_2-TPR measurement was performed by heating the sample from 80 °C to 350 °C at a rate of 10 °C/min under a flow of 10% H_2/Ar (60 mL/min). The temperature was held at 350 °C for 2 hours to record the first H_2 consumption. Subsequently, the system was purged with nitrogen gas (60 mL/min) and left at room temperature for 24 hours without exposure to air. This heating and measurement procedure was repeated under identical conditions for a total of four cycles to assess the H_2 consumption during each step and to determine the reversible interconversion behavior of Cu^+/Cu^+-H species in the catalyst.

The *in situ* H_2 evolution experiment was conducted to verify the reversible interconversion of copper species. A catalyst sample (5–6 mg) was pretreated under a mixed O_2/N_2 flow (12 mL/min O_2 and 48 mL/min N_2) at 400 °C for 2 h, followed by cooling to room temperature under N_2 flow (48 mL/min). Subsequent reduction was performed using 10% H_2 in N_2 (60 mL/min) at 250 °C for 2 h with a ramp rate of 10 °C/min. The sample was then cooled to room temperature under N_2 flow (48 mL/min). Residual hydrogen in the gas phase was purged with N_2 (60 mL/min) until no hydrogen was detected in the effluent. Temperature-programmed desorption (TPD) was carried out by heating the catalyst from room temperature to 400 °C at a rate of 10 °C/min under N_2 flow (60 mL/min) and holding at 400 °C for 30 min. During the experiment, the concentrations of hydrogen (m/z = 2), nitrogen (m/z = 28), and water (m/z = 18) were continuously monitored using a quadrupole mass spectrometer (PFEIFFER VACUUM, PrismaPlus® QMG 220 F with Faraday detector), calibrated with standard gas mixtures.

In situ time-resolved X-ray absorption near edge spectroscopy (in situ TR-XANES) was conducted at beamline BL2.2: TRXAS, Synchrotron Light Research Institute (SLRI), Thailand, to elucidate the oxidation states of Cu species (Cu^0/Cu^+) in the catalysts. The measurements utilized an energy-dispersive monochromator and a position-sensitive detector. Cu K-edge XANES spectra were recorded with an integration time of 2000 ms per scan, averaging 10 scans per sample. The composition of Cu species was quantified through Linear Combination Fitting (LCF) using Athena software, with Cu foil, Cu_2O, CuO, and $CuSO_4$ as reference standards. The LCF fitting was performed in the energy range of 8962–9042 eV, with the edge energy (E^0) fixed. The fitting procedure ensured that the sum of the component fractions equaled unity, achieving an R-factor of <0.05, using the Athena software of XANES spectra.

3.5 Catalytic testing

The selective hydrogenation of methyl palmitate (MP) was performed in a fixed-bed reactor under atmospheric H_2 pressure. Prior to the reaction, the catalyst precursor ($CuMgAlO_x$-pre) was calcined at 550 ℃ under an air flow of 60 mL/min. Subsequently, 0.25 g of the $CuMgAlO_x$ catalyst was packed into the reactor and recalcined at 550 ℃ for 12 h under the same air flow. The catalyst was then reduced under H_2 at a flow rate of 60 mL/min at 250 ℃ for 2 h. Following this, a solution of 10 wt% methyl palmitate in n-dodecane was introduced into the reactor at a feed rate of 2.4 mL/h, with the reaction maintained at 250 ℃ under H_2 flow at 180 mL/min, as depicted in **Figure 3.2**. To prevent product solidification, the reactor outlet was maintained at 70 ℃, and the reaction products were collected and analyzed using gas chromatography (GC-FID) equipped with a DB-1 capillary column. The conversion, yield, selectivity, hydrogenation activity, and alcohol production rate were calculated using the following equations:

$$\text{MP conversion (\%)} = \frac{\text{mol of } MP_0 - \text{mol of } MP_t}{\text{mol of } MP_0} \times 100$$

$$\text{Yield (\%)} = \frac{\text{mol of product } A_t}{\text{mol of } MP_0} \times 100$$

$$\text{Selectivity (\%)} = \frac{\text{Yield of product A (\%)}}{\text{MP conversion (\%)}} \times 100$$

$$\text{Hydrogenation rate (mmol}_{feed}\text{/h·g}_{cat}\text{)} = \frac{\text{mmol of converted MP (mmol/h)}}{\text{Weight of catalyst (g)}}$$

$$\text{Alcohol production rate (h}^{-1}\text{)} = \frac{\text{Weight of hexadecanol production (g/h)}}{\text{Weight of catalyst (g)}}$$

$$\text{Mass balance (\%)} = \frac{\text{Total yield}}{\text{Conversion}} \times 100$$

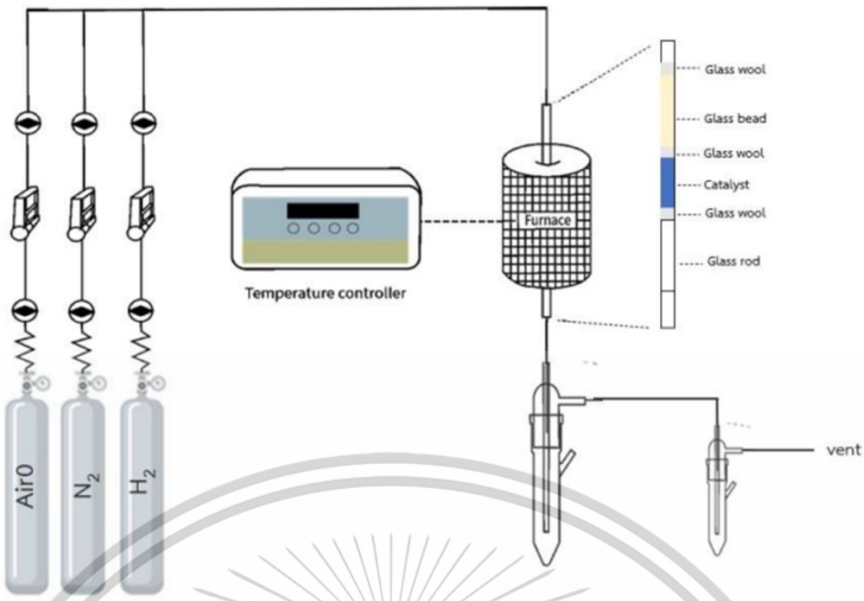

Figure 3.2 The schematic of the reaction rig.

Chapter 4

Main results and discussion

4.1 Catalyst characteristics

The X-ray diffraction (XRD) patterns of Cu-containing layered double hydroxide (LDH) samples, $CuMgAlO_x$-pre (**Figure 4.1**), with varying M^{2+}/M^{3+} molar ratios ranging from 2.2 to 4.8 (**Table 4.1**), exhibited characteristic diffraction peaks typical of LDHs, as previously reported in the literature [58]. The observed 2θ values at 11°, 24°, 35°, 38°, 46°, 60°, and 62° corresponded to the Mg-Al LDH phases at the 003, 006, 009, 105, 108, 110, and 113 diffraction planes, respectively (**Figure 4.2**). No crystalline phases of MgO, CuO, or Al_2O_3 were detected, suggesting that the incorporated Cu^{2+} ions likely substituted Mg^{2+} in the cationic octahedral layers, which are intercalated with anionic layers consisting of carbonate (CO_3^{2-}) and water molecules, as illustrated in Scheme 4.1.

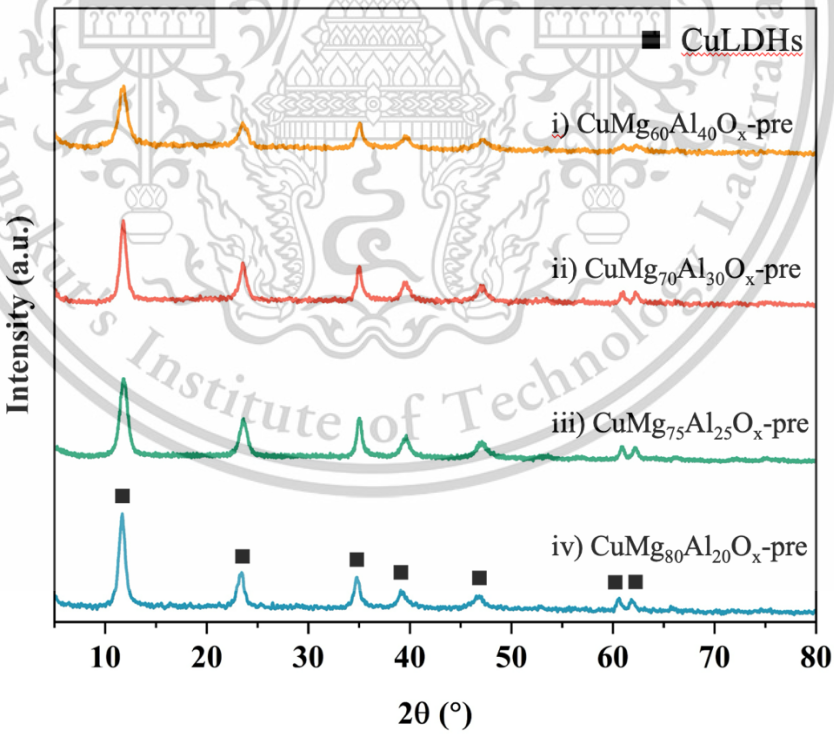

Figure 4.1 XRD patterns of CuLDHs, the mixed metal oxide catalyst precursors.

Table 4.1 Physical and chemical properties of Cu-containing double layered hydroxide samples.

Entry	Catalysts	M_{Cu}[a] (%)	M_{Mg}[a] (%)	M_{Al}[a] (%)	$\%M_{Mg}/\%(M_{Mg}+M_{Al})$	$\%M_{Al}/\%(M_{Mg}+M_{Al})$	CuMg/Al molar ratio	N_2-adsorption S_{BET}[b] (m^2/g)	N_2-adsorption D_p[c] (nm)	N_2-adsorption V_p[c] (cm^3/g)	H_2 consumption (mmol/g)[d]	Cu content (wt.%)[d]	D_{Cu}[e] (%)
1	$CuMg_{60}Al_{40}O_x$	0.27	0.64	0.41	61.16	38.34	2.2	121	35.78	0.69	2.72	17.3	72
2	$CuMg_{70}Al_{30}O_x$	0.27	0.73	0.36	67.30	32.70	2.8	113	37.88	0.59	2.72	17.3	81
3	$CuMg_{75}Al_{25}O_x$	0.29	0.80	0.26	75.30	24.70	4.1	153	31.56	0.63	2.75	17.5	85
4	$CuMg_{80}Al_{20}O_x$	0.27	0.94	0.26	78.87	21.13	4.8	115	36.86	0.92	2.72	17.3	93

[a] Mole of Cu, Mg, and Al Calculated from ICP-OES in ***Table B1****, [b] Determined by N_2 adsorption-desorption analysis (BET), [c] Determined by the BJH method (****Figure 4.2****), [d] Estimated by H_2-TPR, [e] Calculated by conventional dissociative N_2O adsorption.*

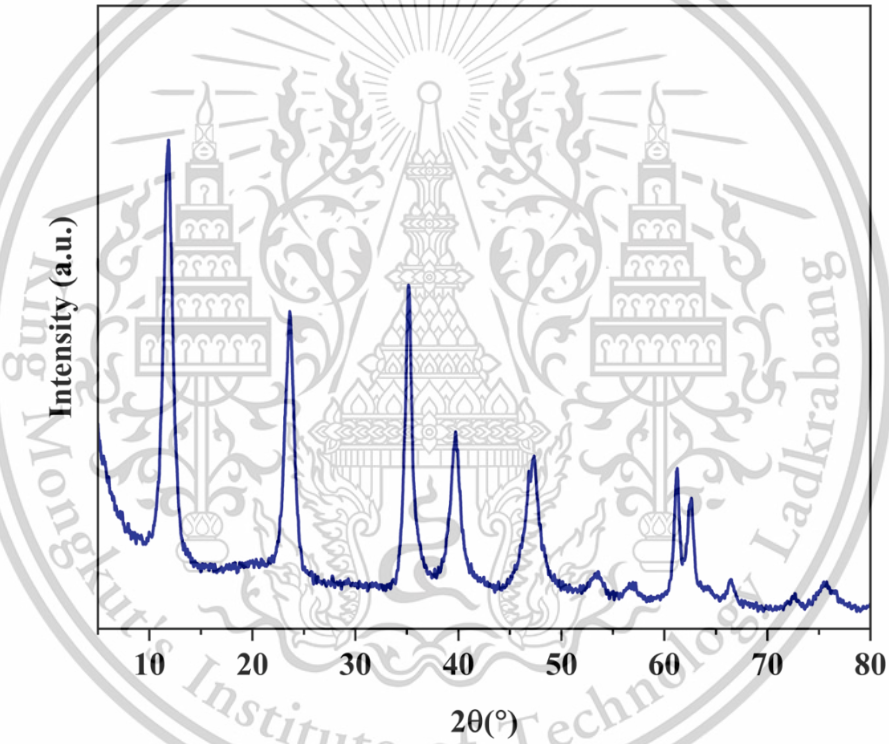

Figure 4.2 XRD patterns of the precursor MgAl-LDHs.

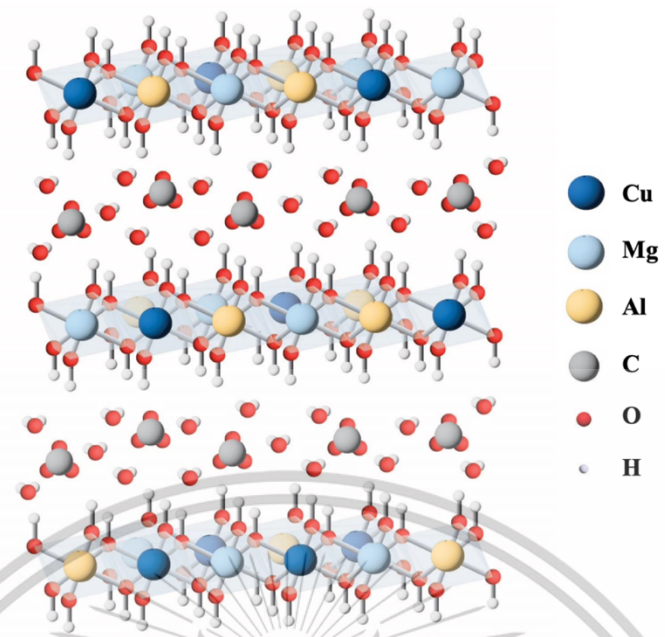

Scheme 4.1 Copper containing layered double hydroxide structure (CuLDHs).

In addition, a slightly broader peak, indicative of a smaller crystallite size, was observed (**Figure 4.1**) as the Al content increased (i.e., as the Mg content decreased) from $CuMg_{80}Al_{20}O_x$ to $CuMg_{60}Al_{40}O_x$ (**Table B1**). Specifically, **Table 4.2** reveals that $CuMg_{60}Al_{40}O_x$ exhibits a crystallite size of approximately 8 nm, while $CuMg_{70}Al_{30}O_x$, $CuMg_{75}Al_{25}O_x$, and $CuMg_{80}Al_{20}O_x$ have crystallite sizes in the range of 11–12 nm. This trend is likely attributed to the lower M^{2+}/M^{3+} molar ratio in $CuMg_{60}Al_{40}O_x$ (2.23, **Table 4.1**), which contains fewer M^{2+} species than conventional LDHs (e.g., $Mg_6Al_2(OH)_{16}CO_3$, with M^{2+}/M^{3+} = 3). Consequently, the octahedral sheets in $CuMg_{60}Al_{40}O_x$ would incorporate more Al^{3+}, leading to cationic layers with a higher positive charge. This would necessitate the presence of more exchangeable anionic species to balance the charge, resulting in higher water retention in the interlayers. Therefore, CuLDHs with higher Al content are expected to exhibit a more labile structure. Supporting this notion, the initial weight loss (50–200 °C), likely due to absorbed water (**Table 4.2** and **Figure 4.3**), increases with increasing Al content ($CuMg_{80}Al_{20}O_x$ < $CuMg_{75}Al_{25}O_x$ < $CuMg_{70}Al_{30}O_x$ < $CuMg_{60}Al_{40}O_x$). The carbonate content, as determined from TGA, between 200–500 °C (decomposition of interlayered carbonates) and 500–700 °C (decomposition of more stable carbonates), is listed in **Table 4.2.** It is noteworthy that the carbonate content across all samples is similar (~24–28 wt.%), suggesting an increase in hydroxide (OH^-) ions to compensate for the cationic layers with higher Al

content. This, in turn, leads to higher water content, likely due to stronger hydrogen bonding within the more highly polarized interlayers. Thus, the water content is inversely related to the $(Cu^{2+} + Mg^{2+})/Al^{3+}$ molar ratio.

Table 4.2 Crystallite size and thermogravimetric analysis.

Entry	Catalysts precursor	Crystallite size[a] (nm)	wt.% loss determined by TGA		
			50-200 °C	200-500 °C	500-700 °C
1	$CuMg_{60}Al_{40}O_x$-pre	8.3	16.0	17.4	3.2
2	$CuMg_{70}Al_{30}O_x$-pre	11.6	13.5	18.7	3.8
3	$CuMg_{75}Al_{25}O_x$-pre	12.3	12.1	18.6	6.3
4	$CuMg_{80}Al_{20}O_x$-pre	11.1	8.1	17.6	3.5

[a] *Determined from XRD using Scherrer method at 2θ = 11°*

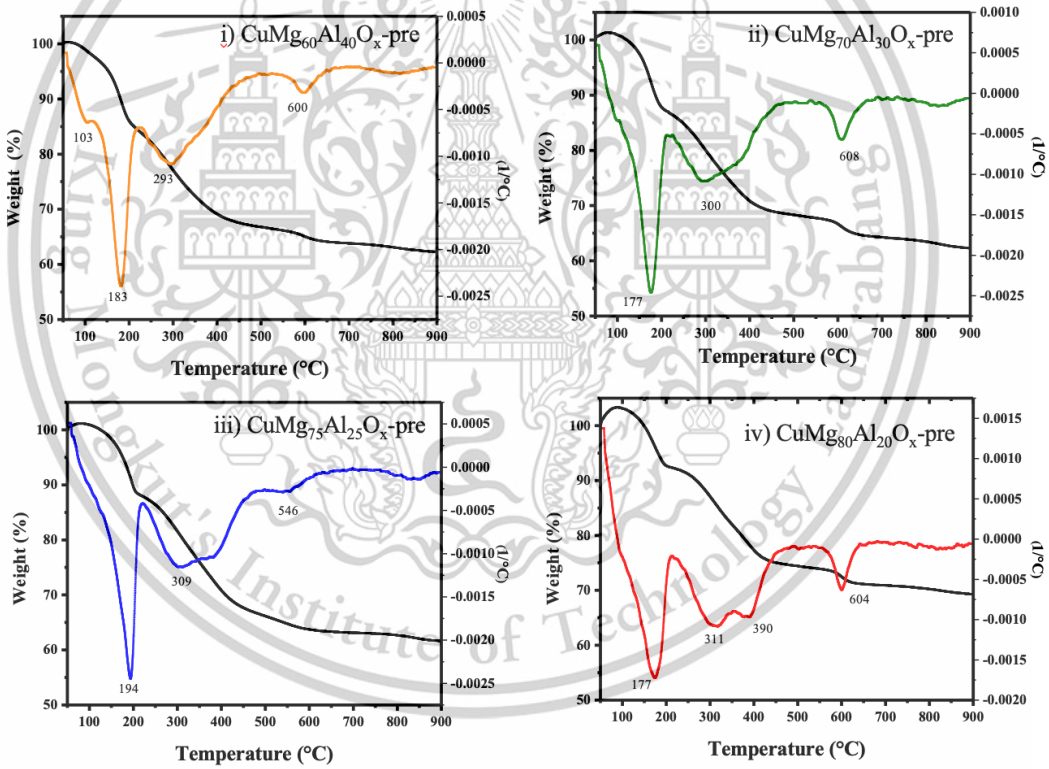

Figure 4.3 TGA profiles (from 50 to 900 °C) of i) $CuMg_{60}Al_{40}O_x$-pre, ii) $CuMg_{70}Al_{30}O_x$-pre, iii) $CuMg_{75}Al_{25}O_x$-pre, and iv) $CuMg_{80}Al_{20}O_x$-pre.

After calcination at 550 °C, the structural collapse of LDHs was observed in all samples (**Figure 4.4a**), accompanied by the expected dehydroxylation of brucite-like layers and decomposition of interlayer CO_3^{2-} species. However, the TGA of the calcined samples confirmed the absence of significant CO_3^{2-} decomposition within

the 200–500 °C range, as shown in Figure 4.5. Only trace amounts (<2 wt.%) of non-layered metal carbonates were detected. The resulting $CuMgAlO_x$ catalysts exhibited surface areas in the range of 100–150 m^2/g, with interparticle voids of 32–36 nm (**Table 4.1, Figure 4.6**) [35,55,59–61]. XRD patterns revealed the presence of periclase (MgO) peaks at 2θ = 35°, 43°, and 64°, with increasing peak intensity correlated with higher M^{2+}/M^{3+} molar ratios ($CuMg_{60}Al_{40}O_x$ < $CuMg_{70}Al_{30}O_x$ < $CuMg_{75}Al_{25}O_x$ < $CuMg_{80}Al_{20}O_x$), consistent with the increasing Mg^{2+} content (Table 1). Notably, no crystalline CuO or Al_2O_3 phases were detected despite the substantial Cu (~17 wt.%) and Al (7–11 wt.%) contents. This suggests a high dispersion of Cu^{2+} and Al^{3+} species within MgO crystallites. Given that Cu^{2+} and Al^{3+} ions in CuLDHs occupy discrete octahedral sites, strong interactions between Cu^{2+} and MgO or Al_2O_3 are likely, effectively inhibiting CuO agglomeration post-calcination, as previously reported in the literature [35].

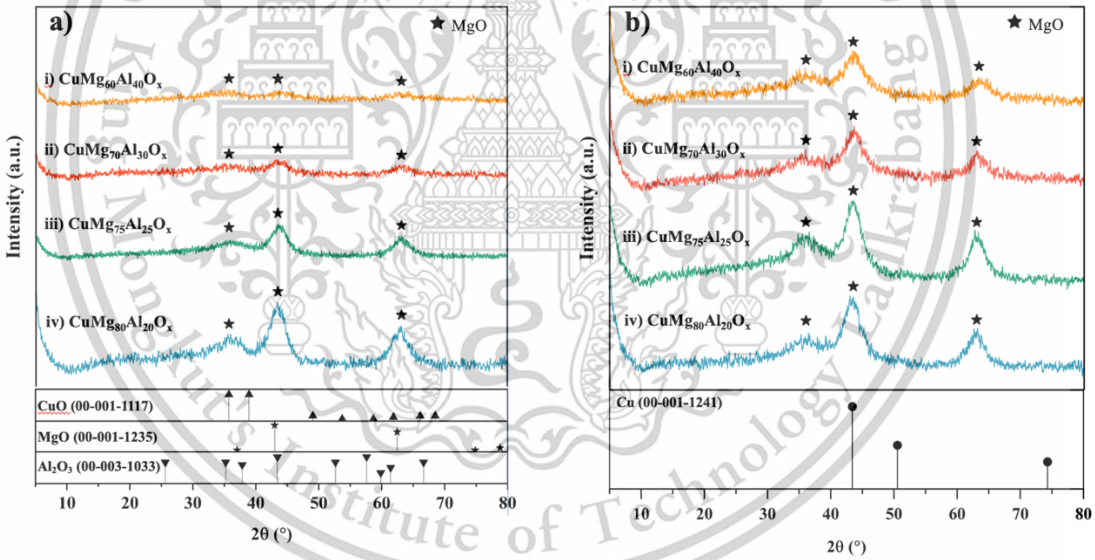

Figure 4.4 XRD patterns of a) calcined and b) reduced mixed metal oxide catalysts.

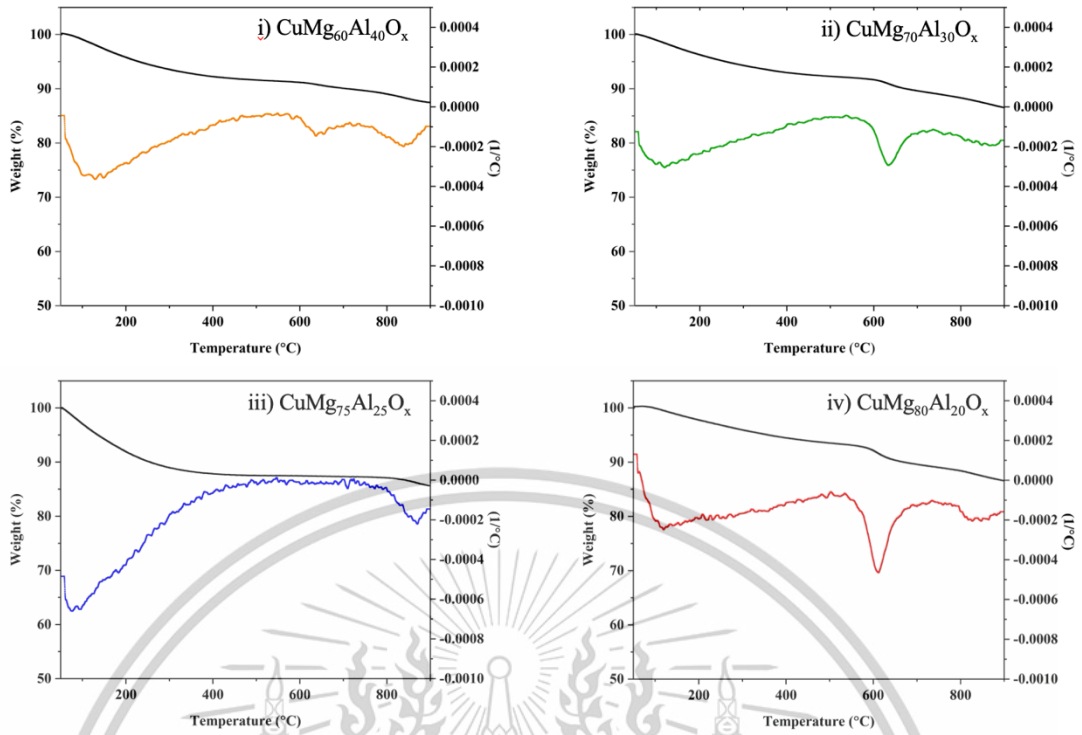

Figure 4.5 TGA profiles (from 50 to 900 °C) of i) $CuMg_{60}Al_{40}O_x$, ii) $CuMg_{70}Al_{30}O_x$, iii) $CuMg_{75}Al_{25}O_x$, and iv) $CuMg_{80}Al_{20}O_x$.

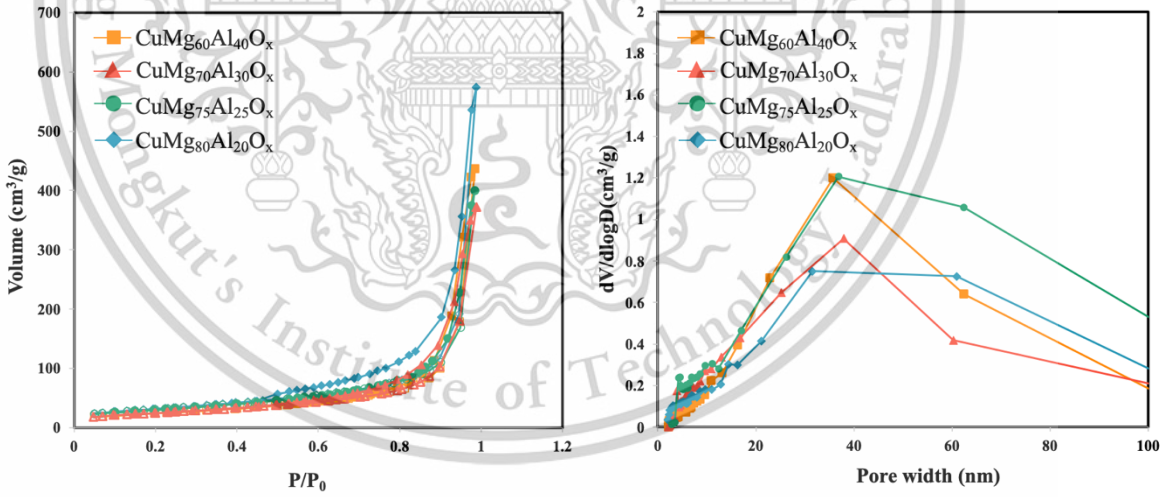

Figure 4.6 Adsorption–desorption isotherm and pore size distribution plot of $CuMg_{60}Al_{40}O_x$, $CuMg_{70}Al_{30}O_x$, $CuMg_{75}Al_{25}O_x$, and $CuMg_{80}Al_{20}O_x$

A higher Al^{3+} content not only reduces the crystallinity of $CuMgAlO_x$ but also significantly suppresses the reducibility of Cu^{2+} species, as evidenced by H_2-TPR profiles (**Figure 4.7**). For Al-rich samples ($CuMg_{60}Al_{40}O_x$ and $CuMg_{70}Al_{30}O_x$), the reduction of Cu^{2+} to Cu^0 occurred at a higher temperature (~253 °C, **Figure 4.7**, i and ii), characterized by a broad reduction peak. In contrast, MgO-rich samples ($CuMg_{75}Al_{25}O_x$ and $CuMg_{80}Al_{20}O_x$) exhibited lower reduction temperatures (~222–225 °C, **Figure 4.7**, iii and iv). This trend suggests a stronger interaction between Cu^{2+} and Al^{3+}, likely forming Cu^{2+}–Al_2O_3 species, compared to the weaker interaction of Cu^{2+} with Mg^{2+} (Cu^{2+}–MgO) [62]. Supporting this observation, Cu impregnated on Al_2O_3 (Cu/Al_2O_3) has been reported to reduce at a higher temperature (~249 °C) [63], whereas Cu doped on MgO (Cu/MgO) exhibits a lower reduction temperature (~215 °C), consistent with the reduction profile shown in **Figure 4.8**.

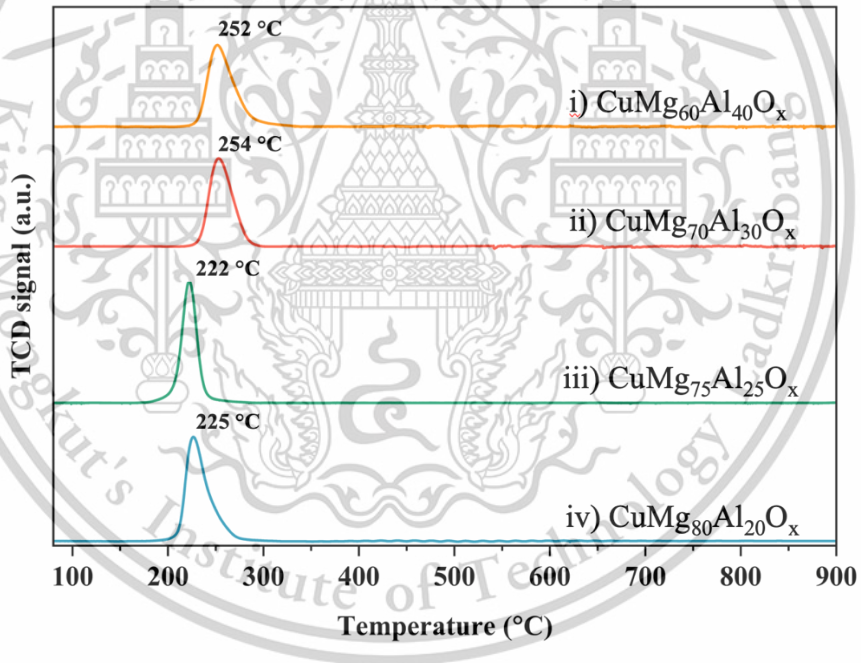

Figure 4.7 H_2-TPR profiles of i) $CuMg_{60}Al_{40}O_x$, ii) $CuMg_{70}Al_{30}O_x$, iii) $CuMg_{75}Al_{25}O_x$, and iv) $CuMg_{80}Al_{20}O_x$.

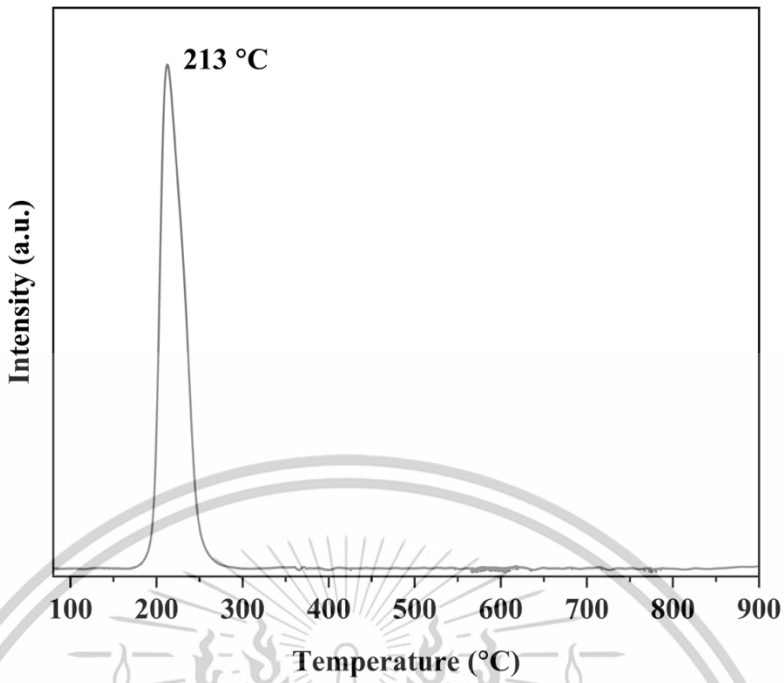

Figure 4.8 H_2-TPR profiles of Cu/MgO.

Despite the higher Cu^{2+} reduction temperatures observed for $CuMgAlO_x$ samples with lower M^{2+}/M^{3+} molar ratios, all samples exhibited highly dispersed Cu nanoparticles. No crystalline metallic Cu phases were detected by XRD, even at a relatively high Cu loading (~17 wt.%, **Figure 4.4b**). TEM analysis further confirmed the presence of ultrafine Cu nanoparticles homogeneously dispersed on the folded sheet-like structures of the mixed oxides (**Figure 4.9**). This suggests that, upon calcination, the lamellar Cu^{2+} oxide structure disintegrates within the collapsed LDH layers due to strong Cu–Al_2O_3 interactions. The resulting fragmented Cu^{2+} oxide sheets are subsequently reduced to Cu nanoparticles within the confined mixed-oxide matrix. Consistent with this hypothesis, all samples exhibited exceptionally high Cu dispersion (>70%), as determined by the N_2O-dissociative reaction (**Figure 4.10**). Moreover, Cu dispersion increased with Mg^{2+} content, ranging from 72% to 93% for $CuMg_{60}Al_{40}O_x$ to $CuMg_{80}Al_{20}O_x$ (Table 1).

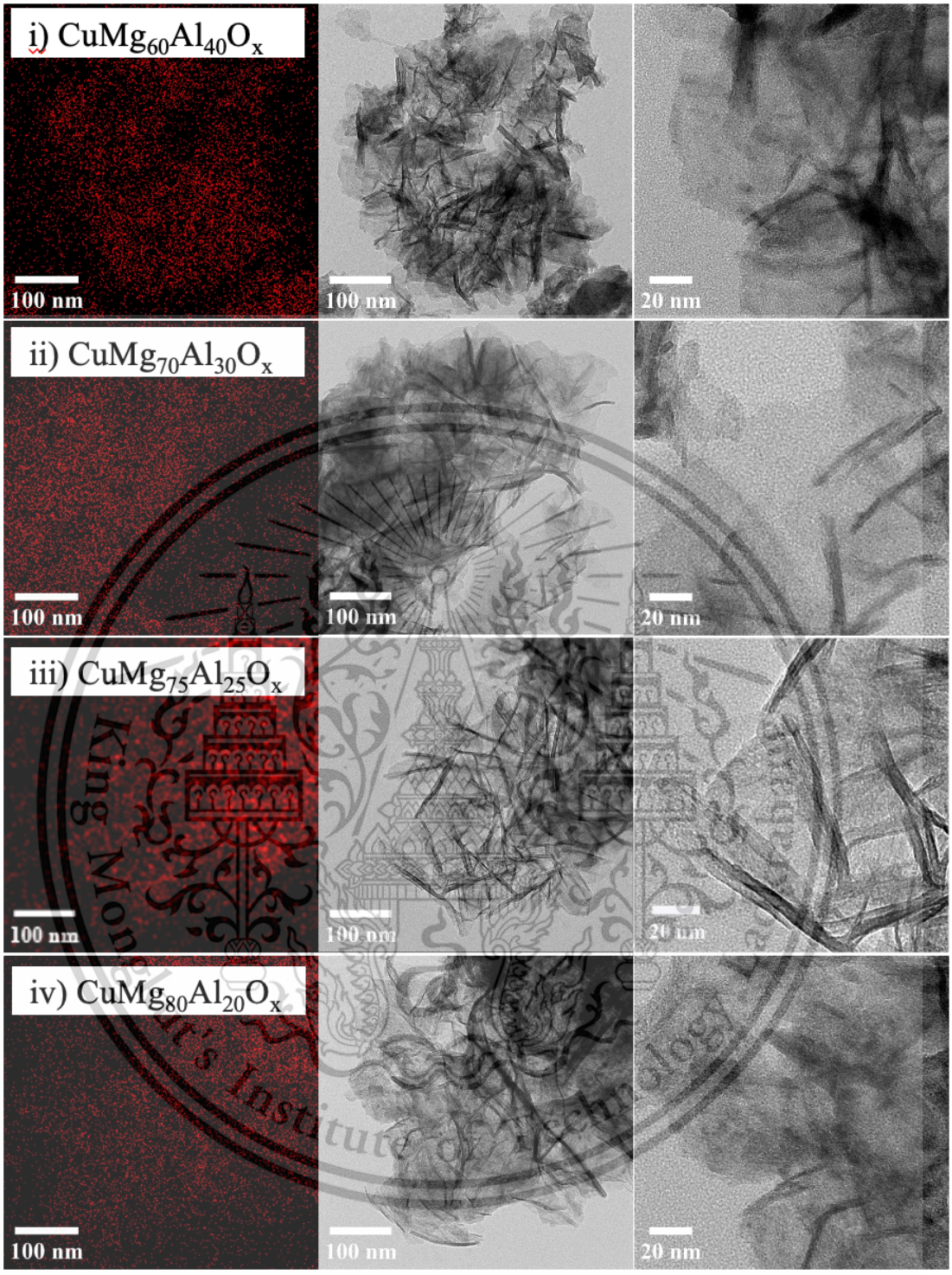

Figure 4.9 TEM images of i) $CuMg_{60}Al_{40}O_x$, ii) $CuMg_{70}Al_{30}O_x$, iii) $CuMg_{75}Al_{25}O_x$, and iv) $CuMg_{80}Al_{20}O_x$.

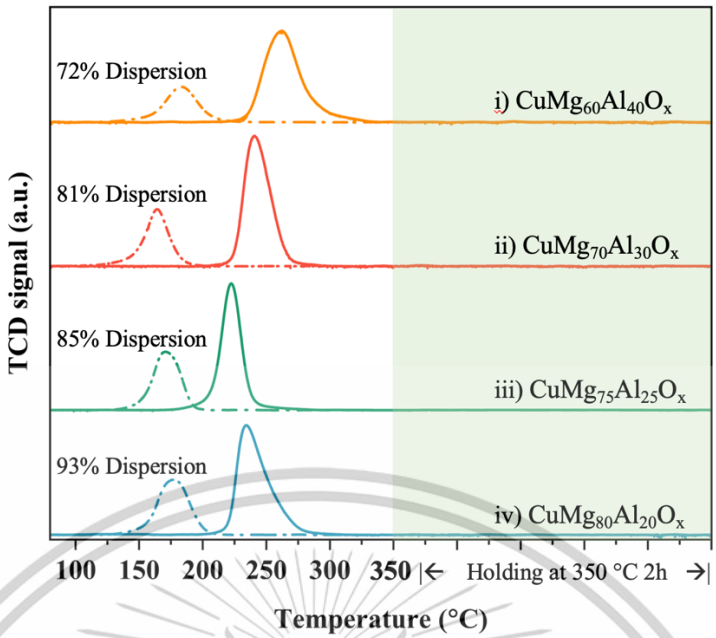

Figure 4.10 The N_2O-dissociative reaction profiles of i) $CuMg_{60}Al_{40}O_x$, ii) $CuMg_{70}Al_{30}O_x$, iii) $CuMg_{75}Al_{25}O_x$, and iv) $CuMg_{80}Al_{20}O_x$ *(first H_2-TPR (solid line) and second H_2-TPR (from 80 to 350 °C) after dissociative N_2O adsorption).*

The total H_2 consumption measured by H_2-TPR corresponds to the Cu loading, assuming a complete reduction of Cu^{2+} to Cu^0 (**Table 4.1**). However, in situ time-resolved X-ray absorption near-edge spectroscopy (in situ TR-XANES) of $CuMg_{75}Al_{25}O_x$ reveals a substantial fraction of residual Cu^+ species after reduction (**Figure 4.11**). The Cu K-edge energy of the reduced sample appears at 8983.2 eV, with a pre-edge feature at 8980.6 eV, closely matching the Cu_2O reference. Linear combination fitting (LCF) analysis confirms that even after reduction at 250 °C for 2 h, $CuMg_{75}Al_{25}O_x$ retains 70% Cu+ species, with only 30% metallic Cu present. Given this high Cu^+ fraction, a significantly lower H_2 consumption would be expected. The apparent discrepancy between H_2 uptake and the persistence of Cu^+ in the reduced sample suggests that the formed Cu^+ species can further interact with H_2, leading to the formation of copper(I) hydride (Cu^+-H) species upon reduction (**Scheme 4.2**). The reduction of Cu^{2+} to Cu^+-H would theoretically consume one equivalent of H_2. However, Cu^+-H species are relatively unstable and can undergo reversible decomposition into Cu^+ and H_2 under an inert atmosphere, a process referred to as “reversible interconversion” [38,39].

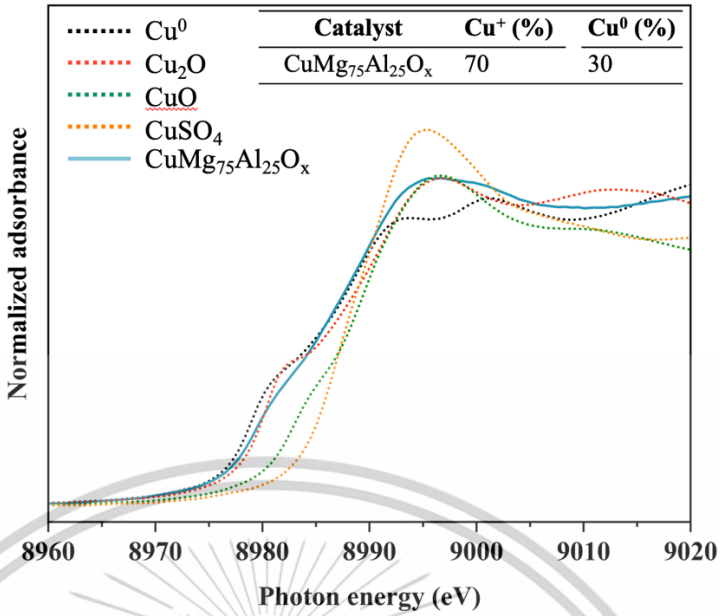

Figure 4.11 *In situ* TR-XANES spectra of reduced $CuMg_{75}Al_{25}O_x$ catalyst and Cu standards (Cu foil (8979.0 eV), Cu_2O (8980.5 eV), CuO (8990.2 eV, square planar geometry, $Cu^{2+}(S_q)$), and $CuSO_4$ (8992.3 eV, octahedral geometry, $Cu^{2+}(O_h)$)

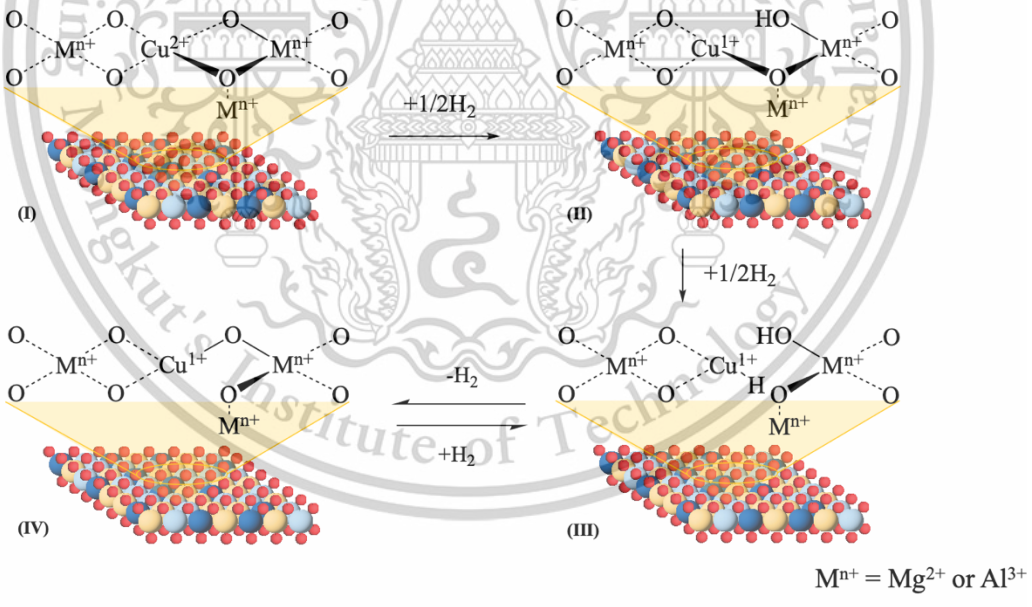

Scheme 4.2 Formation of Cu^+ species and reversible interconversion between Cu^+ and Cu^+-H.

To confirm the reversible interconversion of Cu^{+}/Cu^{+}-H species, consecutive H_2-TPR experiments were conducted. The samples were first reduced under H_2 at 350 °C for 2 h, followed by purging with N_2 at room temperature for 24 h. Without exposure to air, a second H_2-TPR was performed. As anticipated, no secondary H_2 consumption was observed for a typical CuO sample, as a complete reduction to metallic Cu occurred during the initial H_2-TPR (**Figure 4.12i**). In sharp contrast, all $CuMgAlO_x$ samples exhibited a secondary H_2 consumption at a lower temperature (150–160 °C, **Figure 4.12ii–v**) compared to the first reduction step (220–250 °C). This secondary reduction temperature aligns with the reduction of surface Cu_2O (~150 °C), as indicated by N_2O-dissociative reaction profiles (**Figure 4.10**). The observed secondary H_2 consumption, despite the absence of air exposure, suggests that during the first H_2-TPR, the lamellar Cu^{2+} oxide structure undergoes reduction, forming both metallic Cu and Cu^{+}-H species (**Scheme 4.2**). Upon purging under N_2, Cu^{+}-H species (III) decompose into Cu^{+} (IV) and release H_2. Consequently, the secondary H_2 consumption is attributed to the regeneration of Cu^{+}-H species from Cu^{+} at a lower temperature. This reversible process was sustained for at least three consecutive cycles with consistent H_2 consumption (0.91 mmol/g, **Figure 4.13**), further reinforcing the dynamic Cu^{+}/Cu^{+}-H interconversion across all $CuMgAlO_x$ samples. Additionally, the evolution of H_2 from Cu^{+}-H species was directly detected via quadrupole mass spectrometry (Q-MS) during the heating of reduced $CuMg_{75}Al_{25}O_x$, as depicted in **Figure 4.14**.

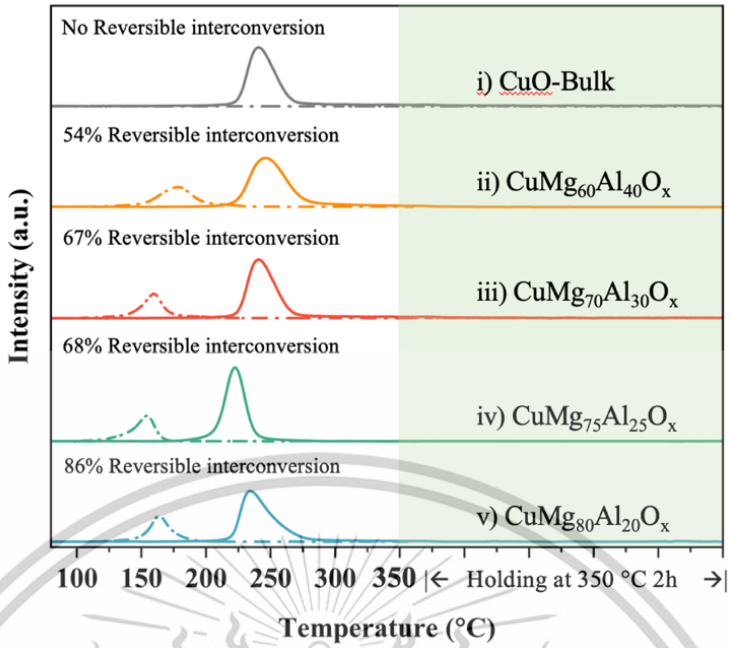

Figure 4.12 Consecutive H_2-TPR profiles of i) CuO-Bulk, ii) $CuMg_{60}Al_{40}O_x$, iii) $CuMg_{70}Al_{30}O_x$, iv) $CuMg_{75}Al_{25}O_x$, and v) $CuMg_{80}Al_{20}O_x$.

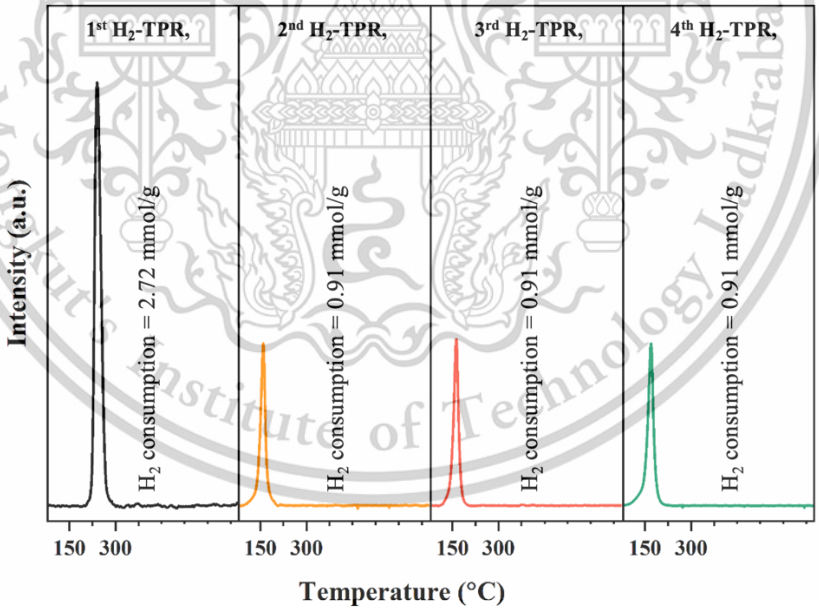

Figure 4.13 The consecutive H_2-TPR profiles of $CuMg_{70}Al_{30}O_x$.

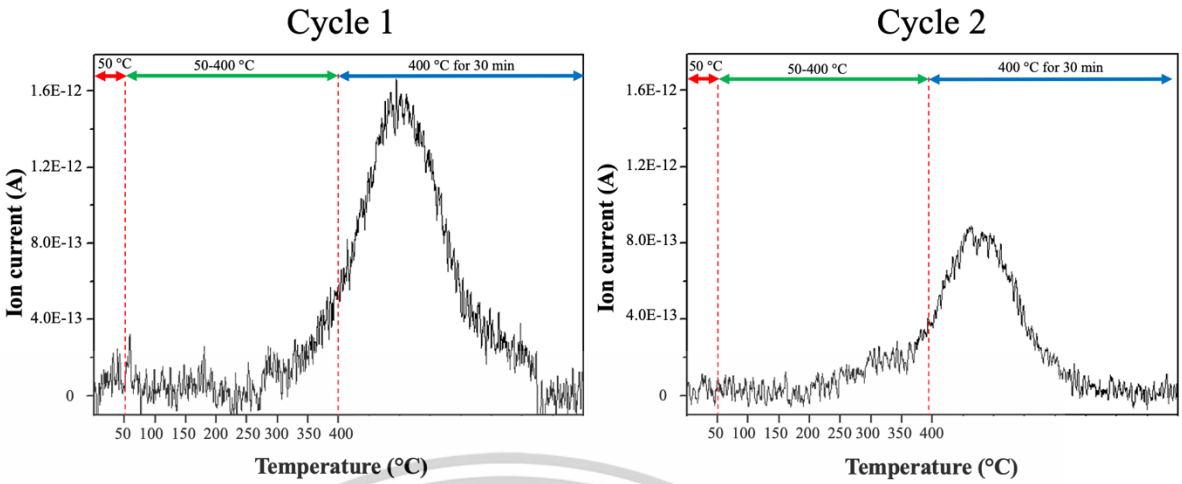

Figure 4.14 H_2 evolution from the reduced $CuMg_{75}Al_{25}O_x$ sample detected by the mass spectrometer (Q-MS).

The amount of Cu^+/Cu^+-H can be quantified from the secondary H_2 consumption (A_2) obtained during the reversible interconversion as represented in eq. (1).

$$\frac{x}{2}H_2 + xCu^+ \rightarrow xCu^+\text{-}H \qquad \text{eq. (1)}$$

The first H_2 consumption (A_1) is the reduction of Cu^{2+} to metallic Cu and Cu^+-H as shown in equation 2, where x is the fraction of Cu^+ in the sample.

$$(x)H_2 + (1\text{-}x)H_2 + Cu^{2+} \rightarrow xCu^+\text{-}H + (1\text{-}x)Cu^0 \qquad \text{eq. (2)}$$

Since, half equivalent of H_2 is consumed for Cu^{2+} to Cu^+, and another half equivalent of H_2 was used for Cu^+ to Cu^+-H. The fraction of Cu^+ in the sample (x) can be calculated from 2 mol of H_2 consumed for Cu^+ to Cu^+-H in eq. (1) divided by the total mol of H_2 consumed for reduction of Cu^{2+} in eq. (2).

$$X = 2A_2/A_1$$

It is noted that the fraction of metallic Cu in the sample can be calculated from 1-x.

During the N_2O-dissociative reaction, not only the surface metallic Cu would be oxidized to $Cu^+_{surface}$ (s), but also the Cu^+-H (x) would be decomposed to Cu^+ as shown in eq. (4)

$$xCuH + (1\text{-}x)Cu^0 \rightarrow xCu^+ + sCu^+_{surface} + (1\text{-}x\text{-}s)Cu^0_{bulk} \qquad \text{eq. (4)}$$

Therefore, the observed secondary H_2 consumption in Figure 5 is not solely derived from the reduction of the partially oxidized Cu surface ($Cu^+_{surface}$) because it

would include the additional H_2 dissociation on remaining Cu^+ to form Cu^+-H species. Accordingly, the hydrogen consumption after N_2O dissociative adsorption (A_3) would be a combination of the hydrogen consumption for the Cu^+-H (A_2) and $Cu^+_{surface}$ as shown in eq. (5).

$$\frac{x}{2}H_2 + \frac{s}{2}H_2 + xCu^+ + sCu^+_{surface} \rightarrow xCuH + sCu^0_{surface} \qquad \text{eq. (5)}$$

Hence, the hydrogen consumption of $Cu^+_{surface}$ (A_s) can be deduced from the H_2 consumed in eq. 5 (A_3) subtracted with the hydrogen consumption of Cu^+ (A_2) as below.

$$A_s = A_3\text{-}A_2$$

Accordingly, the fraction of metallic $Cu_{surface}$ (s) could be derived from the $Cu^+_{surface}$, which can be calculated from 2 mol of A_s, over the total hydrogen consumption of Cu^{2+} in the first H_2-TPR (A_1).

$$S = 2(A_3\text{-}A_2)/A_1$$

The amount of Cu^+, metallic Cu, and $Cu_{surface}$ of all samples can be calculated and summarized in Table 3, the fraction of Cu^+ and metallic Cu obtained from this calculation is also in line with the result from *in situ* TR-XANES (70% Cu^+ and 30% Cu^0 in Figure 6). Therefore, the Cu species remaining in $CuMgAlO_x$ can be determined from the combination of H_2-TPR, N_2O-TPR, and consecutive H_2-TPR with the calculation described above.

Table 4.3 Cu species and corrected Cu metal dispersion of $CuMgAlO_x$ samples.

Entry	Catalysts	Cu^+ (%)	Metallic Cu (%)	
			Total	$Cu_{surface}$
1	$CuMg_{60}Al_{40}O_x$	54	46	18
2	$CuMg_{70}Al_{30}O_x$	66	33	14
3	$CuMg_{75}Al_{25}O_x$	68	32	17
4	$CuMg_{80}Al_{20}O_x$	86	13	7

As presented in **Table 4.3**, all $CuMgAlO_x$ samples exhibit a significant fraction of Cu^+/Cu^+-H species (50–86%). A clear correlation is observed, wherein an increase in Mg^{2+} content corresponds to a higher proportion of Cu^+/Cu^+-H species and a concomitant decrease in metallic Cu species. This finding underscores the pivotal

role of Cu^{2+}-MgO interactions in $CuMgAlO_x$, which facilitate the dispersion of Cu^{2+} species within the MgO lattice, as corroborated by XRD analysis. Such an interaction inhibits the formation of bulk CuO and Cu-Al_2O_3 (copper aluminate) phases upon calcination. Despite the reduced metallic Cu content, an increase in Mg^{2+} content enhances Cu dispersion. This observation further suggests that strong Cu^{2+}-MgO interactions at elevated Mg^{2+} concentrations promote the formation of smaller metallic Cu particles, likely in the form of Cu clusters, as evidenced by the lower reduction temperatures in H_2-TPR (**Figure 4.10**).

4.2 Catalytic activity

The similar hydrogenation activity of $CuMg_{60}Al_{40}O_x$ and $CuMg_{70}Al_{30}O_x$ was observed (~53-54% conversion, **Table 4.4**, entry 1-2), which can be attributed to their similar Cu dispersion (~40%, **Table 4.3**). Hexadecanol (C16-OH) was the primary product, obtained with ~42% yield and ~80% selectivity. In contrast, only minor yields of hexadecanal (C16-al, ~6%), hexadecane (C16-ane, ~6%), and iso-hexadecene (iso-C16-ene, ~6%) were observed. These results highlight the high selectivity of $CuMg_{60}Al_{40}O_x$ and $CuMg_{70}Al_{30}O_x$ for the hydrogenation of fatty acid methyl esters to alcohols. This selectivity can be ascribed to the relatively high Cu^+ content in these catalysts, which facilitates η^1-adsorption of the C=O bond, promoting direct hydrogenation to the corresponding alcohol (**Scheme 4.2**). Moreover, the weak interaction between the alcohol product and Cu^+ enhances desorption, while the presence of Cu^+ suppresses re-adsorption, thereby minimizing dehydration and isomerization to hydrocarbon by-products. Only trace amounts of hexadecanal, the primary intermediate (**Scheme 4.3**), were detected over $CuMg_{60}Al_{40}O_x$ and $CuMg_{70}Al_{30}O_x$, indicating that aldehyde hydrogenation proceeds at a faster rate than ester hydrogenation, consistent with previous reports [64]. However, the small quantities of hexadecane and iso-hexadecene suggest that hexadecanol undergoes dehydration and isomerization, likely catalyzed by acidic surface sites, presumably Al–OH species. Supporting this hypothesis, NH_3-TPD analysis (**Figure 4.15**) revealed only trace acid sites (<10 μmol/g) in $CuMg_{60}Al_{40}O_x$ and $CuMg_{70}Al_{30}O_x$, which may contribute to the minor formation of hydrocarbon by-products.

Table 4.4 Catalytic activity, product yields, and selectivity in hydrogenation of methyl palmitate over $CuMgAlO_x$ catalysts.

Entry	Catalysts	Conversion (%)	Hydrogenation rate (mmol/h.g_{cat})	Alcohol production rate (h^{-1})	Yield (%)				Mass balance (%)	Selectivity (%)			
					C16-OH	C16-al	C16-1-ene	*iso*-C16-ene		C16-OH	C16-al	C16-1-ene	*iso*-C16-ene
1	$CuMg_{60}Al_{40}O_x$	53.7	1.43	41.9	42.0	5.7	2.6	2.9	99	78.1	10.6	4.8	5.3
2	$CuMg_{70}Al_{30}O_x$	52.8	1.41	42.6	42.2	4.6	2.3	2.7	98	79.9	8.8	4.4	5.1
3	$CuMg_{75}Al_{25}O_x$	57.1	1.52	49.3	51.5	2.9	-	1.1	98	90.2	5.2	-	2.0
4	$CuMg_{80}Al_{20}O_x$	30.6	0.81	27.5	27.7	2.0	0.3	0.4	99	90.4	6.7	0.9	1.3

(Reaction condition: 0.25 g of catalyst, 10wt.% methyl palmitate in dodecane, reaction temperature at 250 °C, calcination temperature at 550 °C, reduction temperature at 250 °C, H_2 1 atm (180 mL/min), The activity is at 1 h on stream).

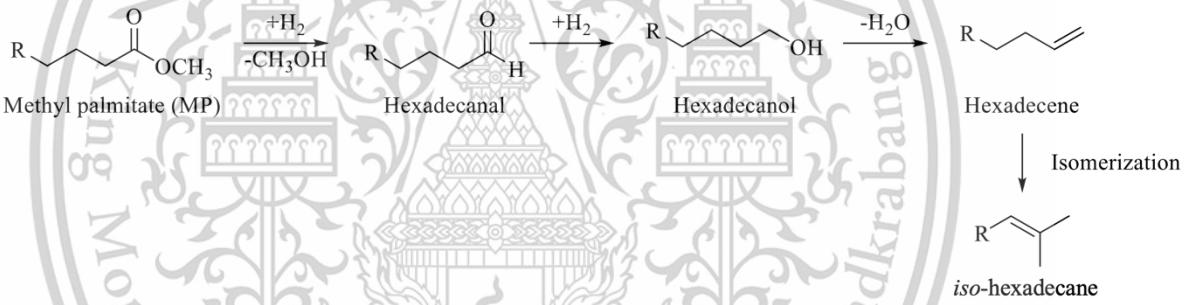

Scheme 4.3 Reaction pathway of methyl palmitate conversion over Cu-based catalysts.

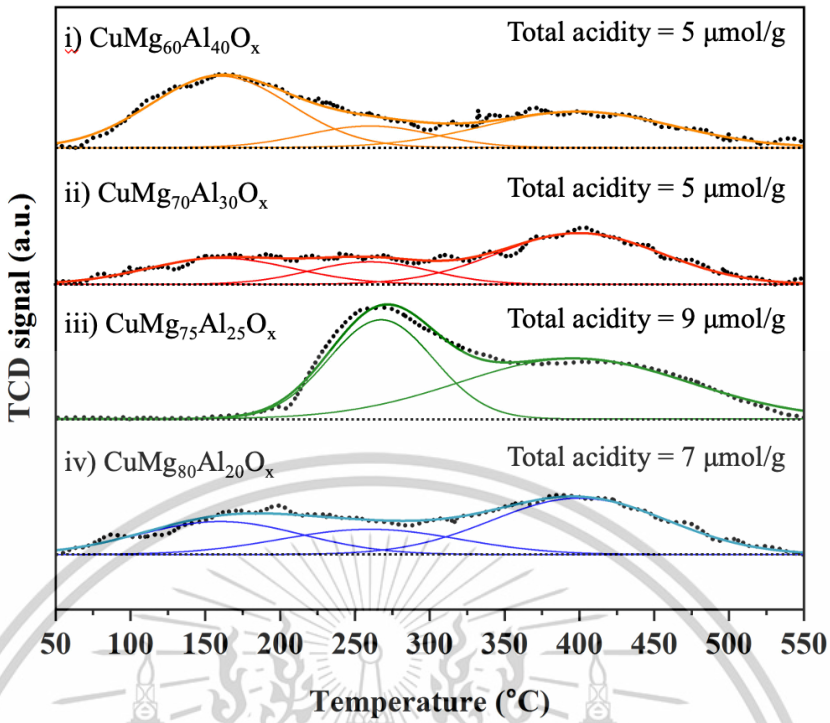

Figure 4.15 NH_3-TPD desorption profiles of reduced samples; i) $CuMg_{60}Al_{40}O_x$, ii) $CuMg_{70}Al_{30}O_x$, iii) $CuMg_{75}Al_{25}O_x$, and iv) $CuMg_{80}Al_{20}O_x$.

An increase in the Mg^{2+}/Al^{3+} ratio enhanced the hydrogenation activity, as evidenced by the higher conversion observed for $CuMg_{75}Al_{25}O_x$ (57%, **Table 4.4**, entry 3) compared to $CuMg_{60}Al_{40}O_x$ and $CuMg_{70}Al_{30}O_x$ (~53–54%). This improvement can be attributed to the higher Cu dispersion in $CuMg_{75}Al_{25}O_x$ (85%, **Table 4.3**, entry 3) relative to $CuMg_{60}Al_{40}O_x$ and $CuMg_{70}Al_{30}O_x$ (72–81%). Consistent with this, a lower yield of C16-al (~3%, down from ~7%) was obtained, suggesting an increased C=O hydrogenation activity. Additionally, $CuMg_{75}Al_{25}O_x$ exhibited a higher yield of C16-OH (~10%) with only trace amounts of C16-ene, likely due to the increased concentration of Cu^+/Cu^+–H species, which facilitate alcohol desorption and prevent re-adsorption.

However, in $CuMg_{80}Al_{20}O_x$, an excess of Cu^+/Cu^+–H species resulted in a decline in activity, likely due to the relatively lower metallic Cu content (~7%). As a result, $CuMg_{80}Al_{20}O_x$ exhibited a lower C16-OH yield (28%) with only trace amounts of C16-ene. These findings suggest that a balance between the active Cu surface ($Cu_{surface}$) and cationic Cu(I) species (Cu^+/Cu^+–H) is crucial for the selective hydrogenation of methyl palmitate to hexadecanol. Given that the reducibility of $CuMgAlO_x$ can be tuned by varying the Mg^{2+}/Al^{3+} ratio (**Figure 4.7**), the fraction of $Cu_{surface}$ and Cu^+ species can be

modulated accordingly (**Table 4.3**). As shown in **Figure 4.16**, the $Cu_{surface}$/Cu(I) ratio plays a key role in hydrogenation selectivity. While cationic Cu(I) species facilitate feed adsorption/activation and alcohol desorption, metallic Cu remains essential for catalytic activity. The hydrogenation conversion increases with the $Cu_{surface}$/Cu(I) ratio up to 0.25, likely due to the enhanced hydrogen dissociation capacity of metallic Cu, complementing the adsorption/activation role of Cu^{+}/Cu^{+}–H species. However, when the $Cu_{surface}$/Cu(I) ratio exceeds 0.25, the overall hydrogenation activity declines, presumably due to an insufficient concentration of Cu+ species for effective methyl palmitate activation, despite the availability of metallic Cu sites.

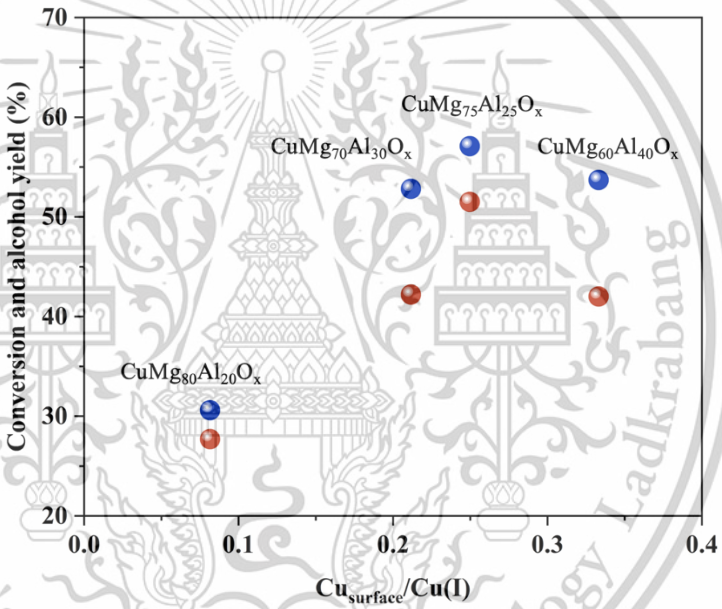

Figure 4.16 Effect of the ratio between active Cu surface ($Cu_{surface}$) and cationic Cu(I) species (Cu^{+}/Cu^{+}-H species) in $CuMgAlO_x$ catalysts on selective hydrogenation of methyl palmitate. *(Reaction condition: 0.25 g of catalyst, 10wt.% methyl palmitate in dodecane, reaction temperature at 250 °C, calcination temperature at 550 °C, reduction temperature at 250 °C, H_2 1 atm (180 mL/min). The activity is at 1 h on stream).*

To elucidate the role of Cu^+ species in the catalytic performance, a $20Cu/SiO_2$ catalyst, prepared via impregnation (lacking Cu^+ species), was evaluated. This catalyst exhibited significantly lower activity, requiring a three-fold higher catalyst loading to achieve a comparable conversion (~53%) to that of $CuMg_{75}Al_{25}O_x$ (**Figure 4.17**). Moreover, $20Cu/SiO_2$ demonstrated only 44% selectivity toward hexadecanol (C16-OH), with a notable formation of side products, particularly C15-ene, a decarbonylation product. In contrast, $CuMg_{75}Al_{25}O_x$ achieved ~90% selectivity for C16-OH, highlighting the crucial role of Cu^+ species in promoting selective hydrogenation while suppressing undesired side reactions.

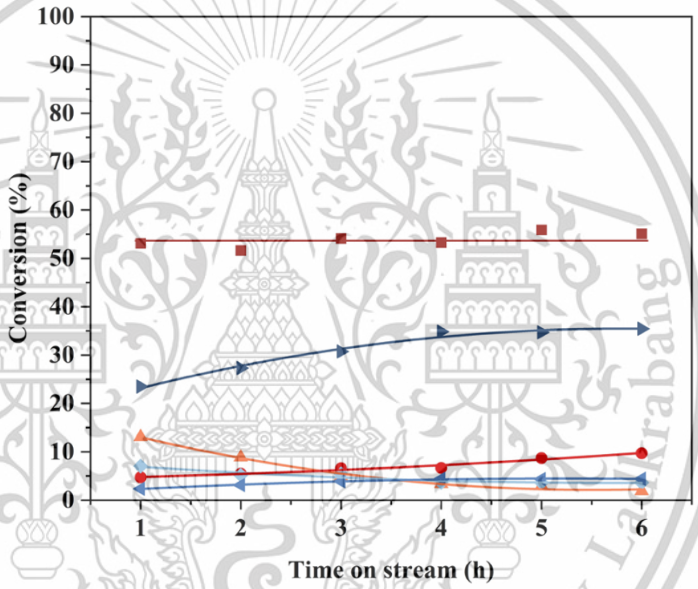

Figure 4.17 Time-on-stream of selective hydrogenation of methyl palmitate using $20Cu/SiO_2$ catalysts (■ Conversion ▶ Hexadecanol ◆ iso-Hexadecene ▲ 1-Hexadecane ◀ C16-nal ● C15), *Reaction conditions: 0.75 g of catalyst, 10wt.% methyl palmitate in dodecane (flow 2 mL/h), reaction temperature at 250 °C, calcination temperature at 550 °C, reduction temperature at 250 °C, H_2 1 atm (180 mL/min), Contact Time 1,334 g.h/mol.*

In a flow reactor, the $CuMg_{75}Al_{25}O_x$ catalyst exhibited significantly higher alcohol selectivity (~90%, **Table 4.5**) compared to other Cu-based catalysts (<60%). While competitive adsorption of alcohols is generally more pronounced in flow systems, the presence of Cu^+/Cu^+-H species in $CuMgAlO_x$ effectively suppresses alcohol re-adsorption, thereby minimizing side reactions such as dehydration and isomerization.

Notably, the alcohol selectivity achieved in this study (~90%) is comparable to that observed in batch reactors (>80%), suggesting that re-adsorption inhibition in the flow system operates similarly to liquid-phase reactions, where ester-feed adsorption predominates. These findings further highlight the critical role of cationic Cu(I) species (Cu^+/Cu^+-H) in governing the selective hydrogenation of esters to alcohols.

Table 4.5 Comparison of selective hydrogenation of methyl palmitate to hexadecanol using various Cu-based catalysts.

Entry	Catalysts	Reaction types	Pressure (bar)	Reaction temperature (° C)	Conversion (%)	Alcohol selectivity (%)	Alcohol production rate (h^{-1})	Ref.
1	$CuMg_{75}Al_{25}O_x$	Fixed-bed	1	250	57.1	90.12	49.3	This work
2	$20Cu/SiO_2$	Fixed-bed	1	250	13.0	60.1	6.9	30
3	20CuPS	Fixed-bed	1	250	73.2	19.2	10.9	30
4	0.05K-rCuPS	Fixed-bed	1	250	54.9	60.1	31.1	31
5	$Cu/m\text{-}ZrO_2$	Batch	75	300	94.6	93.3	167.5	65
6	CuO	Batch	75	300	2.6	80.8	0.3	65
7	1%Pd–Cu(3:1)/ diatomite	Batch	55	250	67.5	85.9	185.7	66
8	$CuCr_2O_4$	Batch	138	280	98.0	95.0	1.1	56

The CuMgAlOx catalysts demonstrate not only high alcohol selectivity but also exceptional stability (Figures 4.18 and 4.19) compared to other Cu-based catalysts such as CuO [65], $CuCr_2O_4$ [56], Cu/SiO_2 [30], 20CuPS [30], 0.05KCuPS [31], 1%Pd–Cu(3:1)/diatomite [66], and $Cu/m\text{-}ZrO_2$ [65], which typically suffer from deactivation. In particular, $CuMg_{75}Al_{25}O_x$ exhibited stable conversion and yields over 100 h (**Figure 4.19**). This stability is attributed to the high content of Cu^+ species (>50%, Table 3) in the catalysts, which undergo reversible interconversion to Cu^+-H species under hydrogen. The reversible Cu^+/Cu^+-H interconversion facilitates hydrogen dissociation and evolution on the catalyst surface, akin to the behavior observed in Pd-based catalysts [67,68]. This dynamic process prevents hydrogen transfer from carbon-containing species (such as esters, alcohols, alkenes, etc.), which could lead to carbonaceous deposit formation, thereby ensuring the catalyst surface remains accessible for feed adsorption and activation.

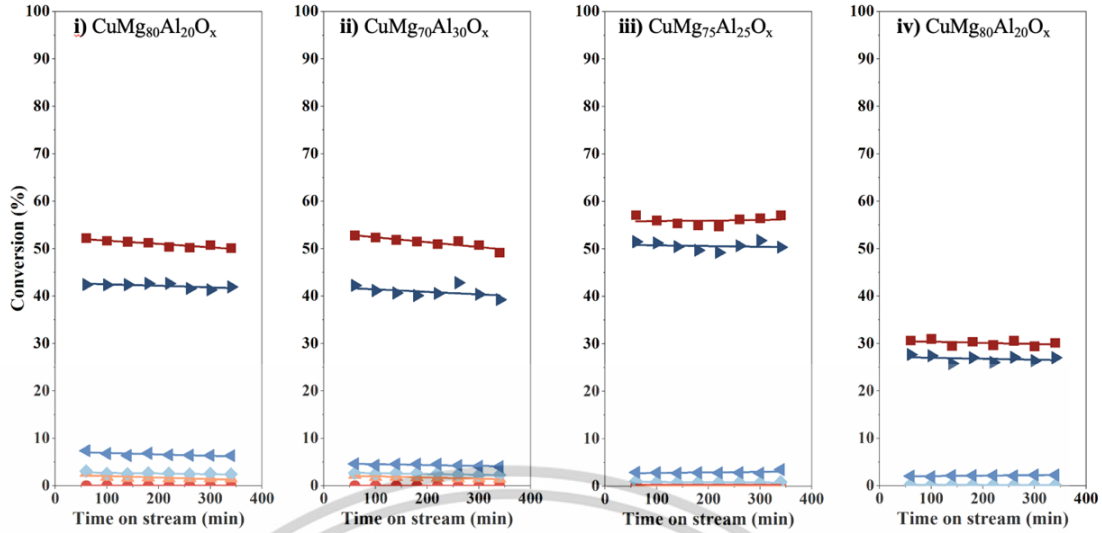

Figure 4.18 Time-on-stream of selective hydrogenation of methyl palmitate using i) $CuMg_{60}Al_{40}O_x$, ii) $CuMg_{70}Al_{30}O_x$, iii) $CuMg_{75}Al_{25}O_x$, and iv) $CuMg_{80}Al_{20}O_x$ (■ Conversion ▶ Hexadecanol ◆ iso-Hexadecene ▲ 1-Hexadecane ◀ C16-nal ● C15). *(Reaction condition: 0.25 g of catalyst, 10wt.% methyl palmitate in dodecane, reaction temperature at 250 °C, calcination temperature at 550 °C, reduction temperature at 250 °C, H_2 1 atm (180 mL/min). The activity is at 1 h on stream.)*

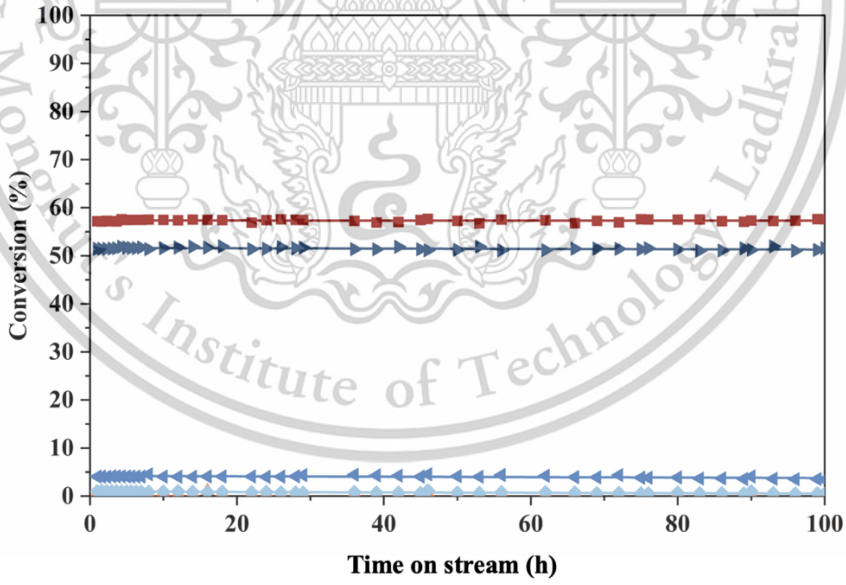

Figure 4.19 Selective hydrogenation of methyl palmitate using $CuMg_{75}Al_{25}O_x$ over 100 h. (■ Conversion ▶ Hexadecanol ◆ iso-Hexadecene ▲ 1-Hexadecane ◀ C16-nal ● C15). *Reaction condition: 0.25 g of catalyst, 10wt.% methyl palmitate in dodecane, reaction temperature at 250 °C, calcination temperature at 550 °C, reduction temperature at 250 °C, H_2 1 atm (180 mL/min).*

Chapter 5
Conclusions and suggestions

5.1 Conclusions

The CuMgAlOx catalysts derived from layered double hydroxides (LDHs) exhibit high selectivity for the hydrogenation of fatty acid methyl esters (FAMEs) to fatty alcohols, achieving up to 92% selectivity in a fixed-bed reactor under atmospheric hydrogen pressure. The lamellar structure of Cu^{2+} oxide in the CuLDH samples is well disintegrated upon calcination due to the strong interaction of Cu^{2+} with the confined mixed oxides, resulting in the rupture of the Cu^{2+} oxide sheets. These ruptured sheets are partially reduced to a mixture of cationic Cu(I) species and highly dispersed Cu nanoparticles. The cationic Cu(I) species exhibit reversible interconversion between Cu^{+} and Cu^{+}-H under hydrogen, facilitated by the strong interaction with the confined mixed oxide layers. A novel approach combining H_2-TPR, consecutive H_2-TPR, and N_2O-dissociative reaction is employed to quantitatively determine the Cu species, including cationic Cu(I) species (Cu^{+}/Cu^{+}-H), metallic Cu, and Cu surface species, with validation by in situ TR-XANES.

As the Mg^{2+} content increases ($CuMg_{60}Al_{40}O_x$ < $CuMg_{70}Al_{30}O_x$ < $CuMg_{75}Al_{25}O_x$ < $CuMg_{80}Al_{20}O_x$), both the amount of cationic Cu(I) species (54% < 66% < 68% < 86%) and Cu dispersion (72% < 81% < 85%, ~93%) increase. The cationic Cu(I) species promote η^1-adsorption and hydrogenation of ester C=O bonds while also preventing alcohol re-adsorption, leading to high selectivity for fatty alcohols. However, hydrogenation activity is governed by the balance between Cu surface species and cationic Cu(I) species. The optimal $Cu_{surface}$/Cu(I) ratio of 0.25 ($CuMg_{75}Al_{25}O_x$) yields a hydrogenation rate of 1.53 mmol/h·gcat and an alcohol production rate of 49.3 h-1. An excess of cationic Cu(I) species ($Cu_{surface}$/Cu(I) ratio < 0.25) results in lower hydrogenation activity due to the limited Cu surface available for hydrogen dissociation. The reversible interconversion between Cu^{+} and Cu^{+}-H facilitates simultaneous hydrogen dissociation and evolution, contributing to the high stability of the catalyst.

5.2 Suggestions

- A comprehensive investigation into the impact of calcination temperature on the ratio of Cu surface ($Cu_{surface}$) to cationic Cu(I) species (Cu^{+}/Cu^{+}-H species) is crucial for deepening our understanding of its role in modulating catalytic activity and redox behavior.

- Definitive evidence of H_2 activation across various catalysts should be obtained through rigorous experimental approaches, such as H_2-D_2 isotopic exchange studies, to gain mechanistic insights and establish performance benchmarks.

References

[1] Fatty Alcohol, https://www.ggcplc.com/en/businesses/fatty-alcohol (accessed March 28, 2024).

[2] fatty alcohol (CHEBI:24026), https://www.ebi.ac.uk/chebi/searchId.do?chebiId=24026 (accessed March 18, 2024).

[3] Fatty Alcohol Market Size, Growth | Analysis Report, 203. https://www.chemanalyst.com/industry-report/fatty-alcohol-market-634 (accessed September 27, 2024).

[4] Fatty Alcohols Market Size, Industry Key Players, & Scenario By 2029. https://www.databridgemarketresearch.com/reports/global-fatty-alcohol-market (accessed September 27, 2024).

[5] Junichi. Kobayashi, Masami. Ishibashi, Bioactive metabolites of symbiotic marine microorganisms, Chem. Rev. 93 (1993) 1753–1769. https://doi.org/10.1021/cr00021a005.

[6] R. Kumar, S.H. Chikkali, Hydroformylation of olefins by metals other than rhodium, J. Organomet. Chem. 960 (2022) 122231. https://doi.org/10.1016/j.jorganchem.2021.122231.

[7] L. Liu, H. Gao, S.-Q. Yang, X.-C. Chen, Y. Lu, Y. Liu, F. Xia, Ir-catalyzed tandem hydroformylation-transfer hydrogenation of olefins with (*trans-/cis-*)formic acid as hydrogen source in presence of 1,10-phenanthroline, J. Catal. 385 (2020) 183–193. https://doi.org/10.1016/j.jcat.2020.03.008.

[8] Y. Zhang, L. Liu, Z. Wang, X. Zhang, X. He, H. Ji, Tandem hydroformylation /hydrogenation of olefins to alcohols using atomically dispersed bifunctional catalysts, Sci. China Chem. 67 (2024) 3706–3711. https://doi.org/10.1007/s11426-024-2135-y.

[9] Home, ICIS Explore (n.d.). https://www.icis.com/explore/ (accessed January 11, 2025).

[10] Market Research Reports & Consulting | Grand View Research, Inc. https://www.grandviewresearch.com/ (accessed January 11, 2025).

[11] S&P Global Commodity Insights, SP Glob. Commod. Insights. https://www.spglobal.com/commodity-insights/en (accessed January 11, 2025).

[12] C. Team, ChemLinked | Global Regulatory & Market Intelligence Expertise, ChemLinked (n.d.). http://www.chemlinked.com/ (accessed January 11, 2025).

[13] L. Boateng, R. Ansong, W.B. Owusu, M. Steiner-Asiedu, Coconut oil and palm oil's role in nutrition, health and national development: A review, Ghana Med. J. 50 (2016) 189–196.

[14] V. Itthibenchapong, A. Srifa, K. Faungnawakij, Heterogeneous Catalysts for Advanced Biofuel Production, in: M. Rai, S.S. da Silva (Eds.), Nanotechnol. Bioenergy Biofuel Prod., Springer International Publishing, Cham, 2017: pp. 231–254. https://doi.org/10.1007/978-3-319-45459-7_11.

[15] F. Beshkar, S. Zinatloo-Ajabshir, M. Salavati-Niasari, Preparation and characterization of the $CuCr_2O_4$ nanostructures via a new simple route, J. Mater. Sci. Mater. Electron. 26 (2015) 5043–5051. https://doi.org/10.1007/s10854-015-3024-1.

[16] R. Rao, A. Dandekar, R.T.K. Baker, M.A. Vannice, Properties of Copper Chromite Catalysts in Hydrogenation Reactions, J. Catal. 171 (1997) 406–419. https://doi.org/10.1006/jcat.1997.1832.

[17] A.A. Khasin, T.M. Yur'eva, L.M. Plyasova, G.N. Kustova, H. Jobic, A. Ivanov, Yu.A. Chesalov, V.I. Zaikovskii, A.V. Khasin, L.P. Davydova, V.N. Parmon, Mechanistic features of reduction of copper chromite and state of absorbed hydrogen in the structure of reduced copper chromite, Russ. J. Gen. Chem. 78 (2008) 2203–2213. https://doi.org/10.1134/S1070363208110418.

[18] M. Snåre, I. Kubičková, P. Mäki-Arvela, K. Eränen, D.Yu. Murzin, Heterogeneous Catalytic Deoxygenation of Stearic Acid for Production of Biodiesel, Ind. Eng. Chem. Res. 45 (2006) 5708–5715. https://doi.org/10.1021/ie060334i.

[19] L. Wang, X. Niu, J. Chen, SiO_2 supported Ni-In intermetallic compounds: Efficient for selective hydrogenation of fatty acid methyl esters to fatty alcohols, Appl. Catal. B Environ. 278 (2020) 119293. https://doi.org/10.1016/j.apcatb.2020.119293.

[20] Z. Dong, J. Zhao, Y. Tian, B. Zhang, Y. Wu, Preparation and Performances of ZIF-67-Derived FeCo Bimetallic Catalysts for CO_2 Hydrogenation to Light Olefins, Catalysts 10 (2020) 455. https://doi.org/10.3390/catal10040455.

[21] R. Krishnapriya, U. Gupta, V.K. Soni, R.K. Sharma, Catalytic conversion of methyl oleate to hydrocarbons: impact of cobalt oxide species integration in SiO_2–Al_2O_3, Sustain. Energy Fuels 4 (2020) 3308–3317. https://doi.org/10.1039/C9SE01221D.

[22] P. Phichitsurathaworn, K. Choojun, Y. Poo-arporn, T. Sooknoi, Deoxygenation of heptanoic acid to hexene over cobalt-based catalysts: A model study for α-olefin production from renewable fatty acid, Appl. Catal. Gen. 602 (2020) 117644. https://doi.org/10.1016/j.apcata.2020.117644.

[23] D. Liu, D. Zemlyanov, T. Wu, R.J. Lobo-Lapidus, J.A. Dumesic, J.T. Miller, C.L. Marshall, Deactivation mechanistic studies of copper chromite catalyst for selective hydrogenation of 2-furfuraldehyde, J. Catal. 299 (2013) 336–345. https://doi.org/10.1016/j.jcat.2012.10.026.

[24] C. Zhang, L. Wang, U.J. Etim, Y. Song, O.M. Gazit, Z. Zhong, Oxygen vacancies in Cu/TiO2 boost strong metal-support interaction and CO_2 hydrogenation to methanol, J. Catal. 413 (2022) 284–296. https://doi.org/10.1016/j.jcat.2022.06.026.

[25] L. Liu, C. Zhao, Y. Li, Spontaneous Dissociation of CO_2 to CO on Defective Surface of Cu(I)/TiO_{2-x} Nanoparticles at Room Temperature, J. Phys. Chem. C 116 (2012) 7904–7912. https://doi.org/10.1021/jp300932b.

[26] A. Chen, X. Yu, Y. Zhou, S. Miao, Y. Li, S. Kuld, J. Sehested, J. Liu, T. Aoki, S. Hong, M.F. Camellone, S. Fabris, J. Ning, C. Jin, C. Yang, A. Nefedov, C. Wöll, Y. Wang, W. Shen, Structure of the catalytically active copper–ceria interfacial perimeter, Nat. Catal. 2 (2019) 334–341. https://doi.org/10.1038/s41929-019-0226-6.

[27] P. Sripada, J. Kimpton, A. Barlow, T. Williams, S. Kandasamy, S. Bhattacharya, Investigating the dynamic structural changes on Cu/CeO_2 catalysts observed during CO_2 hydrogenation, J. Catal. 381 (2020) 415–426. https://doi.org/10.1016/j.jcat.2019.11.017.

[28] Y. Wang, S. Deng, B. Liu, Y. Jin, Mechanistic Understanding on the Role of Cu Species over the CuO_x/TiO_2 Catalyst for CO_2 Photoreduction, ACS Omega 5 (2020) 18050–18063. https://doi.org/10.1021/acsomega.0c01533.

[29] Y. Lin, S.-N. Zhang, Z.-H. Xue, J. Zhang, H. Su, T.-J. Zhao, G. Zhai, X.-H. Li, M. Antonietti, J. Chen, Boosting selective nitrogen reduction to ammonia on electron-deficient copper nanoparticles, Nat. Commun. 10 (2019). https://doi.org/10.1038/s41467-019-12312-4.

[30] W. Prasanseang, K. Choojun, Y. Poo-arporn, A.-L. Huang, Y.-C. Lin, T. Sooknoi, Linear long-chain α-olefins from hydrodeoxygenation of methyl palmitate over copper phyllosilicate catalysts, Appl. Catal. Gen. 635 (2022) 118555. https://doi.org/10.1016/j.apcata.2022.118555.

[31] W. Prasanseang, K. Choojun, Y. Poo-arporn, A.-L. Huang, Y.-C. Lin, E. Chen, H.-H. Lee, P.-W. Chung, T. Sooknoi, Tuning Cu^{+} species/Brønsted acids of copper phyllosilicate by K+ doping for selective hydrogenation of methyl palmitate to hexadecanol, J. Catal. 428 (2023) 115115. https://doi.org/10.1016/j.jcat.2023.115115.

[32] R. Kumar, H.-H. Lee, E. Chen, Y.-P. Du, C.-Y. Lin, W. Prasanseang, T. Solos, K. Choojun, T. Sooknoi, R.-K. Xie, J.-F. Lee, P.-W. Chung, Facile synthesis of the atomically dispersed hydrotalcite oxide supported copper catalysts for the selective hydrogenation of 5–hydroxymethylfurfural into 2,5-bis(hydroxymethyl)furan, Appl. Catal. B Environ. 329 (2023) 122547. https://doi.org/10.1016/j.apcatb.2023.122547.

[33] J. Li, X. Niu, Y. Zhu, Synergistic effect of surface Cu^{0} and Cu^{+} species on improved selective hydrogenation of furfural to furfuryl alcohol over hydrotalcite-derived CuxMg3Al oxides, Appl. Surf. Sci. 635 (2023) 157774. https://doi.org/10.1016/j.apsusc.2023.157774.

[34] A. Yin, X. Guo, W.-L. Dai, K. Fan, The Nature of Active Copper Species in Cu-HMS Catalyst for Hydrogenation of Dimethyl Oxalate to Ethylene Glycol: New Insights on the Synergetic Effect between Cu^{0} and Cu^{+}, J. Phys. Chem. C 113 (2009) 11003–11013. https://doi.org/10.1021/jp902688b.

[35] J. Shi, Y. He, K. Ma, S. Tang, C. Liu, H. Yue, B. Liang, Cu active sites confined in MgAl layered double hydroxide for hydrogenation of dimethyl oxalate to ethanol, Catal. Today 365 (2021) 318–326. https://doi.org/10.1016/j.cattod.2020.04.042.

[36] Y. Liu, R. Zhou, J. Qu, F. Han, S. Zhang, X. Xu, Cu nanoparticles-dispersed Mg-Al layered double hydroxides as efficient catalysts for CO_2 conversion with propargyl alcohols, Appl. Catal. Gen. 630 (2022) 118444. https://doi.org/10.1016/j.apcata.2021.118444.

[37] G. Cui, X. Meng, X. Zhang, W. Wang, S. Xu, Y. Ye, K. Tang, W. Wang, J. Zhu, M. Wei, D.G. Evans, X. Duan, Low-temperature hydrogenation of dimethyl oxalate to ethylene glycol *via* ternary synergistic catalysis of Cu and acid–base sites, Appl. Catal. B Environ. 248 (2019) 394–404. https://doi.org/10.1016/j.apcatb.2019.02.042.

[38] A. Ausavasukhi, S. Suwannaran, J. Limtrakul, T. Sooknoi, Reversible interconversion behavior of Ag species in AgHZSM-5: XRD, 1H MAS NMR, TPR, TPHE, and catalytic studies, Appl. Catal. Gen. 345 (2008) 89–96. https://doi.org/10.1016/j.apcata.2008.04.026.

[39] K. Prakobtham, K. Choojun, P. Promchana, S. Sattayaporn, T. Sooknoi, Role of surface silanols and confinements of siliceous MFI supports on stability of active Ga species for ethane dehydrogenation, Appl. Catal. Gen. 638 (2022) 118625. https://doi.org/10.1016/j.apcata.2022.118625.

[40] T. text provides general information S. assumes no liability for the information given being complete or correct D. to varying update cycles, S.C.D.M. up-to-D.D.T.R. in the Text, Topic: Palm oil industry in Thailand, Statist. https://www.statista.com/topics/12224/palm-oil-industry-in-thailand/ (accessed December 11, 2024).

[41] webadmin, Sustainable and Climate-Friendly Palm Oil Production and Procurement (SCPOPP) in Thailand – Thai-German Cooperation, (2023). https://www.thai-german-cooperation.info/en_US/sustainable-and-climate-friendly-palm-oil-production-and-procurement-scpopp-in-thailand/ (accessed June 9, 2024).

[42] Industry Outlook 2022-2024 : Palm Oil Industry, Krungsri.Com. https://www.krungsri.com/en/research/industry/industry-outlook/agriculture/palm-oil/io/oil-palm-industry-2022-2024 (accessed December 11, 2024).

[43] M.D.F. ltd, Palm Oil Market Size, Share, Analysis & Growth Report, 2032, Mark. Data Forecast. https://www.marketdataforecast.com/market-reports/palm-oil-market (accessed December 11, 2024).

[44] M. Hasanuzzaman, N.A. Rahim, M. Hosenuzzaman, R. Saidur, I.M. Mahbubul, M.M. Rashid, Energy savings in the combustion based process heating in industrial sector, Renew. Sustain. Energy Rev. 16 (2012) 4527–4536. https://doi.org/10.1016/j.rser.2012.05.027.

[45] V.K. Garg, R. Gupta, R. Kumar, R.K. Gupta, Adsorption of chromium from aqueous solution on treated sawdust, Bioresour. Technol. 92 (2004) 79–81. https://doi.org/10.1016/j.biortech.2003.07.004.

[46] Guide to FAME Biodiesel, Crown Oil. https://www.crownoil.co.uk/guides/fame-biodiesel-guide/ (accessed December 11, 2024).

[47] F.D. Gunstone, Fatty acids — Nomenclature, structure, isolation and structure determination, biosynthesis and chemical synthesis, in: Fat. Acid Lipid Chem., Springer US, Boston, MA, 1996: pp. 1–34. https://doi.org/10.1007/978-1-4615-4131-8_1.

[48] Detailed kinetics of fossil and renewable fuel combustion - ScienceDirect,. https://www.sciencedirect.com/science/article/abs/pii/B9780444640871000073?via%3Dihub (accessed December 11, 2024).

[49] Cetyl alcohol, (n.d.). https://go.drugbank.com/drugs/DB09494 (accessed December 10, 2024).

[50] L. Yan, X. Chen, 7 - Nanomaterials for Drug Delivery, in: S.-C. Tjong (Ed.), Nanocrystalline Mater. Second Ed., Elsevier, Oxford, 2014: pp. 221–268. https://doi.org/10.1016/B978-0-12-407796-6.00007-5.

[51] (PDF) Layered double hydroxides - Multifunctional nanomaterials, ResearchGate (2024). https://doi.org/10.2478/s11696-011-0100-8.

[52] W. Zhou, W. Lu, H. Wang, Z. Xia, S. Zhai, Z. Zhang, Y. Ma, M. He, Q. Chen, CuMgAl hydrotalcite as an efficient bifunctional catalyst for the cross-dehydrogenative C–C coupling reactions under mild conditions, Appl. Catal. Gen. 604 (2020) 117771. https://doi.org/10.1016/j.apcata.2020.117771.

[53] T.-T.H. Nguyen, X.-T.T. Nguyen, C.Q. Nguyen, P.H. Tran, Porous metal oxides derived from Cu–Al layered double hydroxide as an efficient heterogeneous catalyst for the Friedel–Crafts alkylation of indoles with benzaldehydes under microwave irradiation, Heliyon 4 (2018) e00966. https://doi.org/10.1016/j.heliyon.2018.e00966.

[54] Y. Zhang, C. Li, C. Yu, T. Tran, F. Guo, Y. Yang, J. Yu, G. Xu, Synthesis, characterization and activity evaluation of Cu-based catalysts derived from layered double hydroxides (LDHs) for DeNO$_x$ reaction, Chem. Eng. J. 330 (2017) 1082–1090. https://doi.org/10.1016/j.cej.2017.08.044.

[55] G. Cui, F. Wang, S. He, M. Wei, Catalytic performance of layered double hydroxide nanosheets toward phenol hydroxylation, RSC Adv 6 (2016). https://doi.org/10.1039/C6RA18917B.

[56] R.D. Rieke, D.S. Thakur, B.D. Roberts, G.T. White, Fatty methyl ester hydrogenation to fatty alcohol part I: Correlation between catalyst properties and activity/selectivity, J. Am. Oil Chem. Soc. 74 (1997) 333–339. https://doi.org/10.1007/s11746-997-0088-y.

[57] T. Chetty, V.D.B.C. Dasireddy, L.H. Callanan, H.B. Friedrich, Continuous Flow Preferential Hydrogenation of an Octanal/Octene Mixture Using Cu/Al_2O_3 Catalysts, ACS Omega 3 (2018) 7911–7924. https://doi.org/10.1021/acsomega.7b01993.

[58] Y. Zeng, T. Zhang, Y. Xu, T. Ye, R. Wang, Z. Yang, Z. Jia, S. Ju, Cu/Mg/Al hydrotalcite-like hydroxide catalysts for *o*-phenylphenol synthesis, Appl. Clay Sci. 126 (2016) 207–214. https://doi.org/10.1016/j.clay.2016.03.017.

[59] L. Dou, H. Zhang, Facile assembly of nanosheet array-like CuMgAl-layered double hydroxide/rGO nanohybrids for highly efficient reduction of 4-nitrophenol, J. Mater. Chem. A 4 (2016) 18990–19002. https://doi.org/10.1039/C6TA08313G.

[60] S. Basąg, Z. Piwowarska, A. Kowalczyk, A. Węgrzyn, R. Baran, B. Gil, M. Michalik, L. Chmielarz, Cu-Mg-Al hydrotalcite-like materials as precursors of effective catalysts for selective oxidation of ammonia to dinitrogen — The influence of Mg/Al ratio and calcination temperature, Appl. Clay Sci. 129 (2016) 122–130. https://doi.org/10.1016/j.clay.2016.05.019.

[61] S. Tanasoi, N. Tanchoux, A. Urdă, D. Tichit, I. Săndulescu, F. Fajula, I.-C. Marcu, New Cu-based mixed oxides obtained from LDH precursors, catalysts for methane total oxidation, Appl. Catal. Gen. 363 (2009) 135–142. https://doi.org/10.1016/j.apcata.2009.05.007.

[62] S. Chen, R. Wojcieszak, F. Dumeignil, E. Marceau, S. Royer, How Catalysts and Experimental Conditions Determine the Selective Hydroconversion of Furfural and 5-Hydroxymethylfurfural, Chem. Rev. 118 (2018) 11023–11117. https://doi.org/10.1021/acs.chemrev.8b00134.

[63] Z. Zhang‡, X. Chen‡, B. Wang, L. Wang, Y. Li, X. Yan, L. Chen, Continuous synthesis of 2,2,6,6-tetramethyl-4-piperidinol over $CuCrSr/Al_2O_3$: effect of Sr promoter, RSC Adv. 13 (2023) 9576–9584. https://doi.org/10.1039/D2RA08306J.

[64] A. Behr, D. Obst, A. Westfechtel, Isomerizing hydroformylation of fatty acid esters: Formation of **ω-**aldehydes, Eur. J. Lipid Sci. Technol. 107 (2005) 213–219. https://doi.org/10.1002/ejlt.200401123.

[65] Efficient Hydrogenation of Methyl Palmitate to Hexadecanol over Cu/m-ZrO_2 Catalysts: Synergistic Effect of Cu Species and Oxygen Vacancies | ACS Catalysis, (n.d.). https://pubs.acs.org/doi/10.1021/acscatal.2c06151 (accessed September 5, 2024).

[66] C. Huang, H. Zhang, Y. Zhao, S. Chen, Z. Liu, Diatomite-supported Pd–M (M = Cu, Co, Ni) bimetal nanocatalysts for selective hydrogenation of long-chain aliphatic esters, J. Colloid Interface Sci. 386 (2012) 60–65. https://doi.org/10.1016/j.jcis.2012.07.032.

[67] W. Liu, Y. Magnin, D. Förster, J. Bourgon, T. Len, F. Morfin, L. Piccolo, H. Amara, C. Zlotea, Size-dependent hydrogen trapping in palladium nanoparticles, J. Mater. Chem. A 9 (2021) 10354–10363. https://doi.org/10.1039/D0TA12174F.

[68] N. Makmeesub, C. Ritvirulh, K. Choojun, T.-H. Chen, Y. Poo-arporn, D.E. Resasco, T. Sooknoi, Reversible Hydrogenation–Dehydrogenation of Acetylpyridine-Pd-MIL-101(Cr) for Chemical Hydrogen Storage, Ind. Eng. Chem. Res. 59 (2020) 17671–17679. https://doi.org/10.1021/acs.iecr.0c02764.

Appendices

Appendix A

Calculation

A1. The calculation for catalyst preparation

The calculation of all $CuMgAlO_x$ layered double hydroxide catalysts prepared by co-precipitation and hydrothermal method.

Molar Mg/Al ratio 2

$$(\text{X mol MgO}) \times \frac{40.299\text{g MgO}}{1\text{ mol MgO}} + ((\text{X}/2)\text{ mol } Al_2O_3) \times \frac{101.946\text{g } Al_2O_3}{1\text{ mol } Al_2O_3} = 2.2511266$$

$$40.299X + 50.973X = 2.2511$$

$$91.272X = 2.2511$$

$$X = 0.0247 \text{ MgO}$$

Weight of CuO, MgO and Al_2O_3 (M.W. of CuO = 79.5459 g/mol, MgO = 40.299 g/mol and Al_2O_3 = 101.946 g/mol

$$CuO = 0.0091 \text{ mol} \times 79.5459 \text{ g/mol} = 0.7243 \text{ g}$$

$$MgO = 0.0246 \text{ mol} \times 40.299 \text{ g/mol} = 0.9939 \text{ g}$$

$$Al_2O_3 = (0.0247 \text{ mol} / 2) \times 101.946 \text{ g/mol} = 1.2572 \text{ g}$$

$$CuO + MgO + Al_2O_3 = 2.9755$$

% Weight

$$MgO = \frac{0.9939}{2.9755} = 34.4044\ \%$$

$$Al_2O_3 = \frac{1.2572}{2.9755} = 42.2522\ \%$$

Convert to NO_3

$$Cu(NO_3)_2 \cdot 3H_2O = 2.2000 \text{ g}$$

$$Mg(NO_3)_2 \cdot 6H_2O = 0.0247 \text{ mol MgO} \times \frac{1 \text{ mol } MgO(NO_3)_2 \cdot 6H_2O}{1 \text{ mol MgO}} \times \frac{256.41 \text{ g } MgO(NO_3)_2 \cdot 6H_2O}{1 \text{ mol } MgO(NO_3)_2 \cdot 6H_2O}$$

$$= 6.3241 \text{ g}$$

$$Al(NO_3)_3 \cdot 9H_2O = \frac{0.0247 \text{ mol MgO}}{2} \times \frac{2 \text{ mol } Al(NO_3)_3 \cdot 9H_2O}{1 \text{ mol } Al_2O_3} \times \frac{256.41 \text{ g } Al(NO_3)_3 \cdot 9H_2O}{1 \text{ mol } Al(NO_3)_3 \cdot 9H_2O}$$

$$= 9.2527 \text{ g}$$

A2. Contact time, W/F

$$W/F = \frac{\text{Weight of catalyst (g)}}{\text{Molar feed rate (mol/h)}}$$

In the reaction using 0.25 g $CuMgAlO_x$, feed: 10% W/V methyl palmitate in dodecane (density of n-dodecane = 0.75 g/mL, Mw = 270.45 g/mol), with a rate of 2.4 mL/h.

The W/F is calculated as follows:

$$W/F = \frac{0.25 \text{ g cat} \times 270.45 \text{ g/mol feed}}{0.75 \text{ g/mL feed} \times 2.4 \text{ mL/h} \times 10\% \text{ feed}}$$

$$= 375 \text{ g•h/mol}$$

In a similar manner, the W/F of catalysts with a different catalyst weight and different %W/V feed is calculated.

A3. Meterial balance

A quantitative description of all materials in the reaction.

$$W/F = \frac{\text{Total yield of product}}{\text{Conversion}} \times 100$$

A4. Corrected area

Corrected area is a mathematical term where the area of interest is divided by the area of the standard.

$$\text{Corrected area of A} = \frac{\text{Area of A}}{\text{External standard}}$$

A5. Cu dispersion (D_{Cu}) calculation

$$D_{Cu} = \frac{2\times(A_2)}{A_1}\times 100$$

$(First\ H_2\ consumption = A_1)$

$(Second\ H_2\ consumption = A_2)$

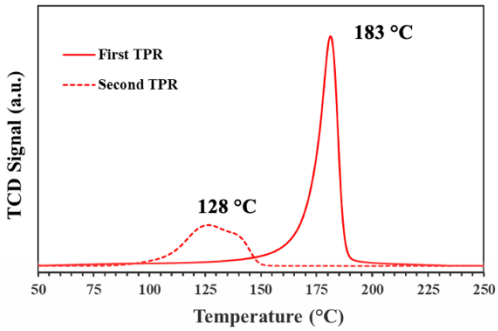

Figure A5. Determination of Cu dispersion using the dissociated N_2O adsorption technique.

Appendix B

Analysis condition

Table B1 The elemental composition of CuMgAlOx catalysts.

Entry	Catalysts	Cu content (wt.%)[a]	Mg content (wt.%)[a]	Al content (wt.%)[a]
1	$CuMg_{60}Al_{40}O_x$	17.2	15.6	11.0
2	$CuMg_{70}Al_{30}O_x$	17.0	17.8	9.6
3	$CuMg_{75}Al_{25}O_x$	18.3	19.5	7.1
4	$CuMg_{80}Al_{20}O_x$	17.3	23.2	6.9

[a] *Determined by ICP-OES*

Author Biography

Name	Chanisara Nooto
Date of Birth	5 June 1998
Address	28/256 Wat Weluwanaram 16, Don Mueang Subdistrict, Don Mueang District, Songprapha Road, Bangkok
Education	(2020) Bachelor of Science Program in Industrial Chemical, King Mongkut's Institute of Technology Ladkrabang
Publication	Reversibly interconverted Cu^{+}/Cu^{+}-H species as active sites for selective hydrogenation of fatty acid methyl esters to fatty alcohol over layered double hydroxide derived $CuMgAlO_x$ catalysts, Chanisara Noot[a], Panalee Chuaykaew, Pawanrat Singthuen, Thanasak Solos, Yardthip Preedawichitkun, Kanyanat Khosukwiwat, Kanokwan Wengwirat, Pratya Promchana, Raju Kuma, Po-Wen Chung, Yingyot Poo-arporn, Wanwisa Limpirat, Kittisak Choojun, and Tawan Sooknoi, Molegular catalysis, 2025